Available online at www.sciencedirect.com
SCIENCE DIRECT®
Journal of Computational Physics 193 (2003) 86–114
JOURNAL OF COMPUTATIONAL PHYSICS
www.elsevier.com/locate/jcp

Accurate mode-separated energy release rates for delamination cracks

Hae-Soo Oh *,[1]

Department of Mathematics, University of North Carolina at Charlotte, 9201 University City Blvd, Charlotte, NC 28223-0001, USA

Received 12 November 2002; received in revised form 23 July 2003; accepted 23 July 2003

Abstract

Babuška and Oh introduced a new approach, called the method of auxiliary mapping (MAM), that can effectively handle singularities in the framework of the *p*-version of the FEM. In this paper, this new approach is generalized so that it can yield highly accurate energy release rates for the cracks in composite materials. The results obtained by this method are more accurate than those obtained by the conventional methods (quarter-point singularity elements). Moreover, it is demonstrated that the mode-separated energy rates of interlaminar cracks of a laminate virtually converge when its layers are of the same material and have different fiber orientations.

Keywords: Method of auxiliary mapping; The *p*-version of the finite element method; Mapping by the blending function method; Mode-separated energy release rate; Interlaminar cracks; Quarter-point singularity elements

1. Introduction

The *h*-version of finite element method (*h*-FEM) is the standard one, where the degree p of the element is fixed, usually at a low level, typically with $p = 1, 2$, or 3 and the accuracy is achieved by properly refining the mesh. On the other hand, the *p*-version of finite element method (*p*-FEM) fixes the mesh and the accuracy is achieved by increasing the degree of polynomial basis functions uniformly or selectively. Recently, Babuška and Oh [1] introduced a new method, called the method of auxiliary mapping (MAM), to deal with the corner singularity in the framework of *p*-FEM. The essence of this method involves locally transforming a region around each singularity to a new domain by using a conformal mapping such as $\xi = z^{\beta}$. Here β is directly determined by the known nature of the singularity in such a way as to locally transform the exact(singular) solution to a smoother function, which can be easily approximated in the new domain by the conventional use of FEM.

* Tel.: +1 704-687-4930; fax: +1-704-687-6415.
E-mail address: hso@uncc.edu (H.-S. Oh).
[1] This research is supported in part by NSF Grant INT-9722699.

0021-9991/$ - see front matter © 2003 Elsevier B.V. All rights reserved.
doi:10.1016/j.jcp.2003.07.025

In this paper, we are concerned with generalizing MAM so that it can yield accurate energy release rates for cracks in heterogeneous materials as well as cracks in homogeneous materials. Main results of this paper include the followings:

(1) A finite element based crack closure method has been shown to be efficient in calculating the strain energy release rate for cracks in homogeneous elastic media [20]. The energy release rates for cracks in homogeneous isotropic materials computed by our method (the mapping technique) in p-FEM are more accurate than those obtained by the conventional method (h-FEM along with the cubic singularity elements) by a factor of 10.

(2) For bimaterial interfacial cracks, because of its oscillatory nature, the strain energy release rates for Mode I and Mode II do not exist [18]. Thus, converged strain energy release rates for Mode I and Mode II cannot be calculated using FEM with the crack closure method. However, in case of interlaminar cracks of a laminate whose layers are of the same material and may have different fiber orientations, the mismatch between two layers is weak; hence, the oscillating factor is very small. It is known that in such cases, Irwin's crack closure integrals defined in Section 2.2 virtually converge ([3–5]: the author is grateful to the referees for these references and pointing out this result). The results obtained by applying our method match very well with this known fact.

This paper is organized as follows: Section 2 introduces the variational form of elasticity equations and the definition of energy released rate. Section 3 develops technical lemmas and methods to obtain highly accurate energy release rates and describes the procedure for implementing the proposed method. Section 4 explains the reasons why the mode-separated energy release rates for interlaminar cracks of the laminates virtually converge when its layers are different only in fiber orientations. In Section 5, in order to demonstrate the effectiveness of the proposed method, this method is applied to compute energy release rates for cracks in homogeneous isotropic materials, cracks in isotropic bimaterials, and interlaminar cracks of fiber-reinforced orthotropic materials. Finally, change of variables and blending mappings for our method are given in Appendix A.

2. Definitions and terminologies

2.1. The equilibrium equations of elasticity

Let $\Omega \subset \mathbf{R}^2$ be a polygonal domain (elastic medium) with boundary $\partial\Omega$ and $H^1(\Omega) = \{w : \|w\|_1 < \infty\}$, where

$$\|w\|_1^2 = \int_\Omega \left[|w|^2 + \left|\frac{\partial w}{\partial x}\right|^2 + \left|\frac{\partial w}{\partial y}\right|^2 \right] \mathrm{d}x\,\mathrm{d}y.$$

In elasticity, the state variable is the displacement vector denoted by $\{u\} = \{u_x(x,y), u_y(x,y)\}^{\mathrm{T}}$ and the flux is the stress tensor denoted by $\{\sigma^{(u)}\} = \{\sigma_x^{(u)}, \sigma_y^{(u)}, \tau_{xy}^{(u)}\}^{\mathrm{T}}$. Let $\{\varepsilon^{(u)}\} = \{\varepsilon_x^{(u)}, \varepsilon_y^{(u)}, \tau_{xy}^{(u)}\}^{\mathrm{T}}$ be the strain tensor. Then the strain–displacement and the stress–strain relations are given by

$$\{\varepsilon^{(u)}\} = [D]\{u\}, \quad \{\sigma^{(u)}\} = [E]\{\varepsilon^{(u)}\}, \tag{1}$$

respectively, where

$$[D] = \begin{bmatrix} \frac{\partial}{\partial x} & 0 & \frac{\partial}{\partial y} \\ 0 & \frac{\partial}{\partial y} & \frac{\partial}{\partial x} \end{bmatrix}^{\mathrm{T}},$$

is the differential operator and $[E] = [E_{ij}]$, $1 \leqslant i, j \leqslant 3$, is the material matrix resulting from the constitutive equation.

The equilibrium equations of elasticity are

$$[D]^{\mathrm{T}}\{\sigma^{(u)}\}(x,y) + \{f\}(x,y) = 0, \quad (x,y) \in \Omega, \tag{2}$$

where $\{f\} = \{f_x(x,y), f_y(x,y)\}^{\mathrm{T}}$ is the vector of internal sources representing the body force per unit area. Introducing the relations (1) into Eq. (2), it can be written as

$$[D]^{\mathrm{T}}[E][D]\{u\}(x,y) + \{f\}(x,y) = 0, \quad (x,y) \in \Omega. \tag{3}$$

Suppose the governing differential equation (3) is subject to the following boundary conditions:

$$[N]\{\sigma^{(u)}\}(s) = \{\tilde{T}\}(s) = \{\tilde{T}_x(s), \tilde{T}_y(s)\}^{\mathrm{T}}, \quad s \in \Gamma_N, \tag{4}$$

$$\{u\}(s) = \{\tilde{u}\}(s) = \{\tilde{u}_x(s), \tilde{u}_y(s)\}^{\mathrm{T}}, \quad s \in \Gamma_D, \tag{5}$$

where $\bar{\Gamma}_N \cup \bar{\Gamma}_D = \partial\Omega$, $\{n_x, n_y\}^{\mathrm{T}}$ is a unit vector normal to the boundary $\partial\Omega$, and

$$[N] = \begin{bmatrix} n_x & 0 & n_y \\ 0 & n_y & n_x \end{bmatrix}. \tag{6}$$

Let $H_D^1(\Omega) = \{w \in H^1(\Omega) : w|_{\Gamma_D} = 0\}$. Then the variational form of Eqs. (3)–(5) is as follows: find $\{u\}$ such that $u_x, u_y \in H^1(\Omega)$, $\{u\} = \{\tilde{u}\}$ on Γ_D and

$$\mathscr{B}(\{u\},\{v\}) = \mathscr{F}(\{v\}) \quad \text{for all } \{v\} \in \mathbf{H}_D^1(\Omega) = \left[H_D^1(\Omega)\right]^2, \tag{7}$$

where

$$\mathscr{B}(\{u\},\{v\}) = \int_\Omega ([D]\{v\})^{\mathrm{T}}[E]([D]\{u\})\,\mathrm{d}x\,\mathrm{d}y, \tag{8}$$

$$\mathscr{F}(\{v\}) = \int_\Omega \{v\}^{\mathrm{T}}\{f\}\,\mathrm{d}x\,\mathrm{d}y + \oint_{\Gamma_N} \{v\}^{\mathrm{T}}\{\tilde{T}\}\,\mathrm{d}s. \tag{9}$$

By the strain energy of the displacement vector $\{u\}$ we mean $\mathscr{U}(\{u\}) = (1/2)\mathscr{B}(\{u\},\{u\})$.

2.2. Mode-separated energy release rate

Consider a crack with area a in a deformable ideally brittle (the plastic deformation is negligible) continuum subjected to arbitrary loading. If the applied load is time independent and the crack grows slowly, then according to the law of conservation of energy, we have

$$\frac{\partial W}{\partial a} = \frac{\partial U}{\partial a} + \frac{\partial \Gamma}{\partial a}, \tag{10}$$

where W is the work performed by the applied loads, U is the elastic strain energy and Γ represents the energy spent in increasing the crack area. If $\Pi = U - W$ denotes the potential energy of the system, Eq. (10) may be put in the form

$$-\frac{\partial \Pi}{\partial a} = \frac{\partial \Gamma}{\partial a}. \tag{11}$$

If γ represents the energy required to form a unit of new material surface, Eq. (10) can be written as [6]

$$G = -\frac{\partial \Pi}{\partial a} = \frac{\partial \Gamma}{\partial a} = 2\gamma, \tag{12}$$

which represents the fracture criterion for the crack growth. The factor 2 appearing on the right-hand side of Eq. (11) refers two new material surfaces formed during the crack growth.

In the fixed-grips loading the surface of the continuum on which the loads are applied is assumed to remain stationary during crack growth. If the work of the body forces is ignored, the work performed by the applied loads vanishes and Eq. (12) takes the form [6]

$$G = -\frac{\partial U}{\partial a} = 2\gamma, \tag{13}$$

which indicates that the energy rate for crack growth is supplied by the existing elastic strain energy of the solid. Thus, G is usually called the *Strain Energy Release Rate.*

Consider the two-dimensional case where the crack extends along its own direction in a self-similar manner. Then the central difference approximation (CDA) for the energy release rate is the following:

$$G \approx \frac{U(a+\Delta) - U(a-\Delta)}{2\Delta} \tag{14}$$

for small values of Δ.

On the other hand, by observing that the work necessary to extend the crack from a to $a+\Delta$ is the same as that necessary to close the crack tip from $a+\Delta$ to a, Irwin [17,20] obtained the energy release rate as

$$\begin{aligned} G = & \lim_{\Delta\to 0} \frac{1}{2\Delta} \int_0^{\Delta} \sigma_y(r,0)[u_y(\Delta - r,\pi) - u_y(\Delta - r,-\pi)]\,\mathrm{d}r \\ & + \lim_{\Delta\to 0} \frac{1}{2\Delta} \int_0^{\Delta} \tau_{xy}(r,0)[u_x(\Delta - r,\pi) - u_x(\Delta - r,-\pi)]\,\mathrm{d}r, \end{aligned} \tag{15}$$

which is known as the virtual crack closure technique (VCCT). Here u_x and u_y represent the x- and the y-component of the displacement vector, respectively.

Two integrals in this formula are called the opening mode (Mode I) and the sliding mode (Mode II), respectively. They are written as

$$G_{\mathrm{I}} \approx \frac{1}{2\Delta} \int_0^{\Delta} \sigma_y(r,0)[u_y(\Delta - r,\pi) - u_y(\Delta - r,-\pi)]\,\mathrm{d}r, \tag{16}$$

$$G_{\mathrm{II}} \approx \frac{1}{2\Delta} \int_0^{\Delta} \tau_{xy}(r,0)[u_x(\Delta - r,\pi) - u_x(\Delta - r,-\pi)]\,\mathrm{d}r. \tag{17}$$

However, due to the oscillatory nature of the stress and displacement fields at the crack tip, the modes are inseparable for most composite materials. In other words, for the interfacial cracks between dissimilar materials, each of the integrals in VCCT usually do not converge because of the nature of the interpenetration of the crack surfaces near the crack tip. Of course, the sum of two integrals (total energy release rate) does converge.

2.3. Total energy release rates

In [27], the central difference approximation (14) was discarded because of the following reasons: (a) the computation involves differences of large numbers divided by a small number and hence the resulting value is not accurate; (b) this procedure involves two runs of a FE code.

However, in this paper, Eq. (14) is employed to estimate the total energy release rate. Moreover, it is shown that CDA approach (14) is even better than the VCCT approach in computations of total energy release rates. In fact, unlike the *p*-FEM with respect to geometric mesh, the CDA approach is not realistic for the *h*-version of the FEM(*h*-FEM) because it is too expensive to make Δ sufficiently small.

2.4. Δ-Dependence of the numerical definitions of mode-separated energy release rates

Applying the VCCT to compute the energy release rate, from Eqs. (16) and (17), numerical definitions of G_{I} and G_{II} obviously depend on the size of Δ. However, the Δ-dependence are as follows:

- (Homogeneous materials) if a cracked body consists of homogeneous material, the line integrals of the definitions are of the form

$$\frac{1}{2\Delta}\int_0^{\Delta} \mathcal{O}(\sqrt{\Delta - x}/\sqrt{x})\,\mathrm{d}x.$$

  And it becomes

$$\int_0^{\pi/2} \mathcal{O}(\cot t)\sin 2t\,\mathrm{d}t,$$

  by the substitution $x = \Delta\sin^2 t$. Hence, the mode-separated energy release rates (16) and (17) are Δ-independent.
- (Heterogeneous materials) On the other hand, if a crack is along the interface of two dissimilar materials, displacement functions and stress tensor are oscillating singular near the crack tip and the integrand is of the form $\mathcal{O}([\sqrt{\Delta - x}/\sqrt{x}]\ \cdot \sin(\varepsilon\log\sqrt{\Delta - x})\cos(\varepsilon\log x))$, where ε is known as the oscillating factor. Because of the oscillating behavior, the mode-separated energy release rates G_{I} and G_{II} are Δ-dependent; hence, the convergence should be determined. Actually, it has been known in the computational mechanics community [2,12,19,21,26] that G_{I} and G_{II} of bimaterial interface cracks do not converge.

Conventional methods to compute the energy release rates use nodal forces ahead of the crack tip and relative displacements behind the crack tip (Irwin's argument) with quarter-point singular elements in the framework of the *h*-FEM. On the other hand, our method is to use MAM (introduced in Section 3.2 and Appendix A) in the framework of the *p*-FEM and the technical Lemmas for line integral developed in Section 3.3 (however, this method is not effective for the *h*-FEM with linear basis functions).

3. A new approach to compute energy release rates

For brevity, we consider G_{I} in two-dimensional case. Let us consider the line integral

$$\frac{1}{2\Delta}\int_0^{\Delta} \sigma_y(x,0)\delta u_y(x-\Delta,0)\,\mathrm{d}x, \tag{18}$$

where $\delta u_y(x-\Delta,0) = [u_y(\Delta - r,\pi) - u_y(\Delta - r,-\pi)]$ is the relative displacement. Suppose the stress tensor σ_y and the y-displacement u_y are oscillating singular functions. Then in order to get accurate energy release rate, we have to overcome the following problems:

- Low accuracy of FE solutions in the presence of the singularities and the poor approximability due to the oscillating factor ε.
- Low accuracy in numerical integrations of singular functions. The FE solutions of σ_y and δu_y obtained by our method are singular.

3.1. Auxiliary mappings

In what follows, Ω_S denotes a small neighborhood of a the crack tip and $\Omega_R = \Omega \cap [\Omega_S]^C$. Then Ω_S and Ω_R are called a singular subregion and a regular subregion, respectively. In order to deal with those problems mentioned above, we introduce an auxiliary mapping that maps the neighborhood Ω_S in the x–y plane into the domain $\hat{\Omega}_S$ in the $\hat{x}$–$\hat{y}$ plane. Now, we define the *power auxiliary mapping* (PAM) $\varphi^{\beta}_{\text{pow}} : \hat{\Omega}_S \to \Omega_S$ by

$$\varphi^{\beta}_{\text{pow}}(\hat{x},\hat{y}) = (\hat{r}^{\beta}\cos(\beta\hat{\theta}), \hat{r}^{\beta}\sin(\beta\hat{\theta})), \tag{19}$$

where $(\hat{r},\hat{\theta})$ is the polar coordinates of $(\hat{x},\hat{y})$. The constant $\beta \geqslant 1$ is a positive real number, which will be called the mapping size of the auxiliary mapping.

For example, suppose $\beta = 2$, then we have

$$\left[r^{1/2}\sin(0.15\log r)\right] \circ \varphi^{2}_{\text{pow}}(\hat{r},\hat{\theta}) = \hat{r}\sin(0.3\log\hat{r}).$$

One clearly see that the transformed functions by the auxiliary mapping is much smoother than the original function.

3.2. New method for accurate economical FE solutions

Finite element meshes $\Delta(\Omega)$ of Ω are partitions of the domain Ω into triangular or quadrilateral elements $E_k, k = 1,\ldots,N(\Delta)$. Elemental mappings are bijective mappings Ψ_k from the reference element $\Omega^{(*)}_{\text{st}}$ onto the kth element $E_k \in \Delta(\Omega)$, where $\Omega^{(*)}_{\text{st}}$ stands for either the reference quadrilateral element $\Omega^{(q)}_{\text{st}}$ or the reference triangular element $\Omega^{(t)}_{\text{st}}$ (see Fig. 1 and Appendix A.1.3 for definitions). Then the finite element space $S^p(\Omega,\Delta,\{\Psi_k\})$ for FE-solutions is determined by

- the finite element meshes $\Delta(\Omega)$ of Ω,
- the elemental mappings $\Psi_k : \Omega^{(*)}_{\text{st}} \to E_k$ for $k = 1,\ldots,N(\Delta)$,
- the basis functions that span $P_p(\Omega^{(*)}_{\text{st}})$ which denotes the set of all polynomials of degree $\leqslant p$ defined on $\Omega^{(*)}_{\text{st}}$.

This is, the finite element space is

$$S^p(\Omega,\Delta,\{\Psi_k\}) = \{u : \|u\|_1 < \infty, u(\Psi_k(\xi,\eta)) \in P_p(\Omega^{(*)}_{\text{st}}) \text{ for all } E_k \in \Delta(\Omega)\},$$

where $\{\Psi_k\}$ is the vector of elemental mappings from the reference element $\Omega^{(*)}_{\text{st}}$ onto the elements E_k.

In standard FEM, the elemental mappings Ψ_k usually are of polynomial type (smooth). However, unlike the standard one, in the proposed method (MAM), we assign singular bijective elemental mappings Ψ^S_k (defined below) to those elements surrounding the crack tips. This is the only difference between the standard FEM and our method.

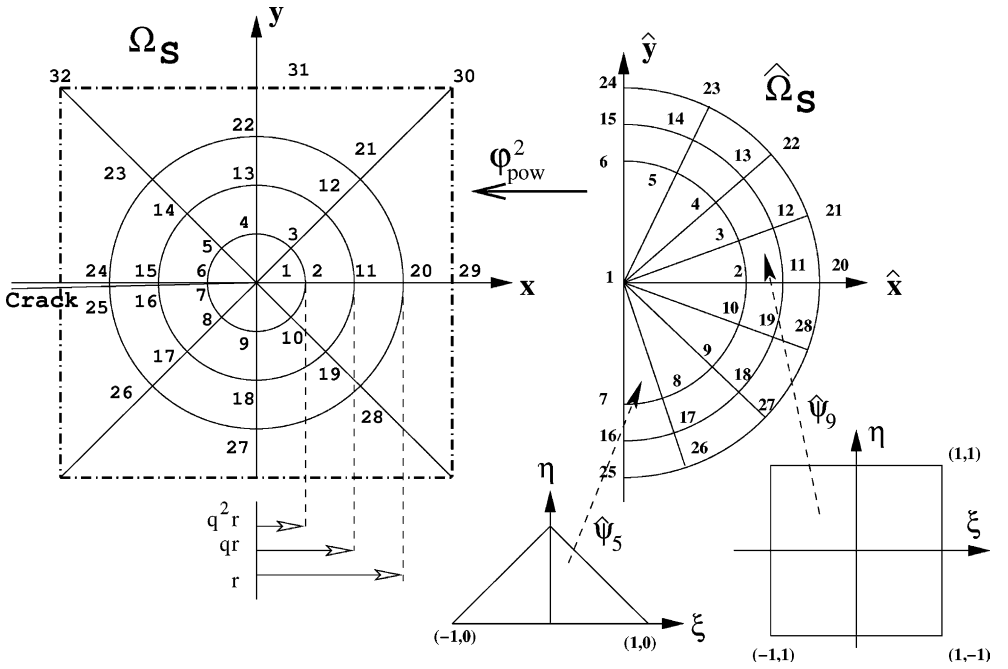

Fig. 1. Schemes of neighborhood Ω_S of crack tip, the mapped neighborhood $\hat{\Omega}_S$, the singular elemental mappings $\Psi_5^S(\xi,\eta) = (\varphi_{pow}^2 \circ \hat{\Psi}_5)(\xi,\eta)$ and $\Psi_9^S(\xi,\eta) = (\varphi_{pow}^2 \circ \hat{\Psi}_9)(\xi,\eta)$. Here $r = h_0/2$.

The FE solution vector $\{u\}_{fe}$ of Eq. (7) is in $[S^p(\Omega,\Delta,\{\Psi_k\})]^2$. The dimension of the vector space $[S^p(\Omega,\Delta,\{\Psi_k\})]^2$ is called the *Number of Degree of Freedom.* Let us note that in *the p-version of FEM*, the mesh $\Delta(\Omega)$ of the domain Ω is fixed and only the degree p of the basis polynomials is increased to obtain the desired accuracy.

3.2.1. Construction of meshes for the neighborhoods of the crack tips

Let $\Omega_S = \{(r,\theta) : r \leqslant h_0/2\} \subset [-h_0,h_0] \times [-h_0,h_0]$ be a neighborhood of the crack tip, where h_0 is the layer thickness. For example, partition Ω_S into eight triangular elements and 16 quadrilateral elements as shown in Fig. 1. More specifically,

(i) let $r_1 = h_0/2,\ r_2 = r_1 q,\ r_3 = r_1 q^2$, where the ratio q is $(\sqrt{2}-1)^2 = 0.17$ which is known to be an optimal choice for a geometric mesh for the p-FEM (Chapter 4 of [23]).

(ii) Let $\hat{r}_i = \sqrt{r_i},\ i = 1,2,3.$ Then $\hat{P}_1 = (0,0),\ \hat{P}_j = (\hat{r}_3,\ (j-2)\times\pi/8),\ j = 2,3,4,5,6; \hat{P}_j = (\hat{r}_3, (j-7)\pi/8 - \pi/2),\ j = 7,8,9,10;\quad \hat{P}_j = (\hat{r}_2,\ (j-11)\times\pi/8),\ j = 11,\ldots,15;\ \hat{P}_j = (\hat{r}_2,\ (j-16)\pi/8 - \pi/2),\ j = 16,\ldots,19;\ \hat{P}_j = (\hat{r}_1,\ (j-20)\times\pi/8),\ j = 20,\ldots,24;\ \hat{P}_j = (\hat{r}_1,\ (j-25)\pi/8 - \pi/2),\ j = 25,\ldots,28$ are the polar coordinates for nodes in $\hat{\Omega}_S$.

It is possible to construct a geometric mesh for Ω_S with straight sides as usual. However, the corresponding sides in $\hat{\Omega}_S$ are still curved. For example, the parametrization of the curved side $(\hat{x}_1^{(1)}, \hat{y}_1^{(1)})$ of Eq. (A.6) is given by

$$\left(\hat{x}_1^{(1)}, \hat{y}_1^{(1)}\right)(\xi) = \left(\varphi_{pow}^2\right)^{-1}[\Psi_1(\xi,0)], \tag{20}$$

where Ψ_1 is the usual bilinear elemental mapping from $\Omega_{st}^{(t)} \to E_1$.

3.2.2. The construction of singular elemental mappings for those elements in the neighborhood of the crack tip

Let E_k be the elements in Ω_S and $\hat{E}_k = (\varphi^2_{\text{pow}})^{-1}(E_k)$ be the corresponding elements in $\hat{\Omega}_S$. Let $\hat{\Psi}^{(*)}_k$ be the conventional elemental mapping of blending type from the reference element $\Omega^{(*)}_{\text{st}}$ to $\hat{E}_k$ defined by Eqs. (A.6) and (A.7). Now, we define the singular elemental mappings $\Psi^S_k : \Omega^{(*)}_{\text{st}} \to E_k$, by the composition of the power auxiliary mapping and the conventional elemental mapping $\hat{\Psi}^{(*)}_k$:

$$E_k \overset{\varphi^2_{\text{pow}}}{\leftarrow} \hat{E}_k \overset{\hat{\Psi}^{(*)}_k}{\leftarrow} \Omega^{(*)}_{\text{st}}.$$

Let us note that if $\bar{f}(s,t) \in P_p(\Omega^{(*)}_{\text{st}})$, then $[\bar{f} \circ (\Psi^S_k)^{-1}](x,y)$ become singular shape functions on E_k which resemble the crack singularity.

3.2.3. Finite element space for MAM

Let $\Delta(\Omega) = \Delta(\Omega_S) \cup \Delta(\Omega_R)$ denotes a specific mesh on $\Omega = \Omega_S \cup \Omega_R, \overset{\circ}{\Omega}_S \cap \overset{\circ}{\Omega}_R = \varnothing$, where $\Delta(\Omega_S)$ is the mesh in Fig. 1 and $\Delta(\Omega_R)$ denotes a quasi-uniform mesh on Ω_R that is compatible with the mesh $\Delta(\Omega_S)$. Suppose $\{\Psi_k : k = 1, \ldots, N(\Delta)\}$ is the vector of elemental mappings assigned to each element $E_k \in \Delta(\Omega)$ by the following rules:

- the singular elemental mapping Ψ^S_k to elements $E_k \in \Delta(\Omega_S)$(the singular zone Ω_S); and
- the conventional polynomial elemental mapping Ψ_k to the elements $E_k \in \Delta(\Omega_R)$ (the regular zone Ω_R).

In the constructions of regular elemental mappings of blending type (Appendix A.1.3), the elemental mapping for eight quadrilateral elements E_k, $k = 25, \ldots, 32$ in $[-h_0, h_0] \times [-h_0, h_0]$ (those elements surrounding Ω_S in Fig. 1) and the singular elemental mappings Ψ^S_k of the outermost eight quadrilateral elements E_k, $k = 17, \ldots, 24$ of the singular zone Ω_S agree along their common circular sides (see Fig. 1).

Thus, we obtain *exactly and minimally conforming* (p. 38 of [23]) finite element space.

3.2.4. Implementing this method

The accurate FE solutions are obtained by solving the linear systems whose stiffness matrices and load vectors are computed in the following ways.

Local stiffness matrices. By (7), (A.1), (A.2), and Lemma A.1, the (i,j) component of the stiffness matrix is as follows:

$$A_{ij} = \mathscr{B}(\{\Phi\}_i, \{\Phi\}_j) = \int_\Omega ([D]\{\Phi\}_j)^{\mathrm{T}}[E]([D]\{\Phi\}_i)\,\mathrm{d}x\,\mathrm{d}y, \tag{21}$$

$$= \sum_{k=1}^{n} \int_{E_k} ([D]\{\Phi\}_j)^{\mathrm{T}}[E]([D]\{\Phi\}_i)\,\mathrm{d}x\,\mathrm{d}y, \tag{22}$$

$$= \sum_{k=1}^{n} \int_{E_k} (\nabla\Phi_j)^{\mathrm{T}} \begin{bmatrix} E_{k_1 s_1} & E_{k_1 s_2} \\ E_{k_2 s_1} & E_{k_2 s_2} \end{bmatrix} (\nabla\Phi_i)\,\mathrm{d}x\,\mathrm{d}y, \tag{23}$$

where $\Phi_j \in S^p(\Omega, \Delta(\Omega), \{\Psi_k\})$. From the construction of basis function Φ_j through the vector $\{\Psi_k\}$ of the elemental mappings (master element approach), we have

$$\Phi_j|_{E_k}(x,y) = \begin{cases} \overline{\mathscr{N}}^{(k)}_j\left(\left[\Psi^S_k\right]^{-1}(x,y)\right) & \text{if } E_k \subset \Omega_S \text{ (singular zone)}, \\ \overline{\mathscr{N}}^{(k)}_j([\Psi_k]^{-1}(x,y)) & \text{if } E_k \subset \Omega_R \text{ (regular zone)} \end{cases} \tag{24}$$

for a basis function $\overline{\mathscr{N}}^{(k)}_j \in P_p(\Omega^{(*)}_{\text{st}})$. Hence, it follows from Lemma A.2 that the corresponding component in local stiffness matrix on the element E_k is as follows:

- If E_k is an element in the singular zone Ω_S,

$$\begin{aligned}
A_{ij}|_{E_k} &= \int_{E_k} (\nabla_x \Phi_j)^{\mathrm{T}} \begin{bmatrix} E_{k_1 s_1} & E_{k_1 s_2} \\ E_{k_2 s_1} & E_{k_2 s_2} \end{bmatrix} (\nabla_x \Phi_i)\, \mathrm{d}x\, \mathrm{d}y \\
&= \int_{\Omega_{\mathrm{st}}^{(*)}} \left| J\left(\Psi_k^S\right) \right| \left(J\left(\Psi_k^S\right)^{-1} \nabla_\xi \overline{\mathscr{N}}_j^{(k)} \right)^{\mathrm{T}} \cdot \begin{bmatrix} E_{k_1 s_1} & E_{k_1 s_2} \\ E_{k_2 s_1} & E_{k_2 s_2} \end{bmatrix} \cdot \left(J\left(\Psi_k^S\right)^{-1} \nabla_\xi \overline{\mathscr{N}}_i^{(k)} \right) \mathrm{d}\xi\, \mathrm{d}\eta \\
&= \int_{\hat{E}_k} \left| J\left(\varphi_{\mathrm{pow}}^2\right) \right| \nabla_{\hat{x}} \left(\overline{\mathscr{N}}_i^{(k)} \circ \hat{\Psi}_k^{-1} \right)^{\mathrm{T}} \cdot \left(J\left(\varphi_{\mathrm{pow}}^2\right)^{-1} \right)^{\mathrm{T}} \cdot \begin{bmatrix} E_{k_1 s_1} & E_{k_1 s_2} \\ E_{k_2 s_1} & E_{k_2 s_2} \end{bmatrix} \\
&\quad \cdot \left(J\left(\varphi_{\mathrm{pow}}^2\right)^{-1} \right) \nabla_{\hat{x}} \left(\overline{\mathscr{N}}_i^{(k)} \circ \hat{\Psi}_k^{-1} \right) \mathrm{d}\hat{x}\, \mathrm{d}\hat{y} \\
&= \int_{\hat{E}_k} \left(\nabla_{\hat{x}} \left(\overline{\mathscr{N}}_j^{(k)} \circ \hat{\Psi}_k^{-1} \right) \right)^{\mathrm{T}} \cdot \begin{bmatrix} Q_{11} & Q_{12} \\ Q_{21} & Q_{22} \end{bmatrix} \cdot \nabla_{\hat{x}} \left(\overline{\mathscr{N}}_i^{(k)} \circ \hat{\Psi}_k^{-1} \right) \mathrm{d}\hat{x}\, \mathrm{d}\hat{y} \\
&= \int_{\Omega_{\mathrm{st}}^{(*)}} |J(\hat{\Psi}_k)| \left(J(\hat{\Psi}_k)^{-1} \nabla_\xi \overline{\mathscr{N}}_j^{(k)} \right)^{\mathrm{T}} \cdot \begin{bmatrix} Q_{11} & Q_{12} \\ Q_{21} & Q_{22} \end{bmatrix} \cdot \left(J(\hat{\Psi}_k)^{-1} \nabla_\xi \overline{\mathscr{N}}_i^{(k)} \right) \mathrm{d}\xi\, \mathrm{d}\eta,
\end{aligned}$$

where

$$\begin{cases}
(\hat{x}_k, \hat{y}_k) = \hat{\Psi}_k(\xi, \eta), \\
\hat{r} = \sqrt{\hat{x}_k^2 + \hat{y}_k^2}, \\
\hat{\theta} = \sin^{-1} \frac{\hat{y}}{\hat{r}}, \\
t = (1 - \beta)\hat{\theta}, \text{ where } \beta = \frac{1}{2} \text{ is the mapping size}, \\
Q_{11} = E_{k_1 s_1} \cos^2 t + E_{k_2 s_2} \sin^2 t - (E_{k_2 s_1} + E_{k_1 s_2}) \sin t \cos t, \\
Q_{12} = (E_{k_1 s_1} - E_{k_2 s_2}) \sin t \cos t - E_{k_2 s_1} \sin^2 t + E_{k_1 s_2} \cos^2 t, \\
Q_{21} = (E_{k_1 s_1} - E_{k_2 s_2}) \sin t \cos t - E_{k_1 s_2} \sin^2 t + E_{k_2 s_1} \cos^2 t, \\
Q_{22} = E_{k_1 s_1} \sin^2 t + E_{k_2 s_2} \cos^2 t + (E_{k_1 s_2} + E_{k_2 s_1}) \sin t \cos t,
\end{cases}$$

$\Psi_k^S(\xi, \eta) = (\varphi_{\mathrm{pow}}^2 \circ \hat{\Psi}_k)(\xi, \eta)$ is the singular elemental mapping and $\hat{\Psi}_k(\xi, \eta) = (\hat{x}^k(\xi, \eta), \hat{y}^k(\xi, \eta))$ is the regular elemental mapping of blending type from $\Omega_{\mathrm{st}}^{(*)}$ to $\hat{E}_k$ (defined by (A.6) and (A.7)). In other words, $A_{ij}|_{E_k}$ is computed by using the transformed bilinear form (A.4).

- If E_k is an element in the regular zone Ω_R,

$$\begin{aligned}
A_{ij}|_{E_k} &= \int_{E_k} (\nabla_x \Phi_j)^{\mathrm{T}} \begin{bmatrix} E_{k_1 s_1} & E_{k_1 s_2} \\ E_{k_2 s_1} & E_{k_2 s_2} \end{bmatrix} (\nabla_x \Phi_i) \\
&= \int_{\Omega_{\mathrm{st}}^{(*)}} |J(\Psi_k)| \left(J(\Psi_k)^{-1} \nabla_\xi \overline{\mathscr{N}}_j^{(k)} \right)^{\mathrm{T}} \cdot \begin{bmatrix} E_{k_1 s_1} & E_{k_1 s_2} \\ E_{k_2 s_1} & E_{k_2 s_2} \end{bmatrix} \cdot \left(J(\Psi_k)^{-1} \nabla_\xi \overline{\mathscr{N}}_i^{(k)} \right) \mathrm{d}\xi\, \mathrm{d}\eta,
\end{aligned}$$

where Ψ_k is the conventional elemental mapping.

Local Load vectors. The computation of the local load vector on the element E_k is similar. Let

$$b_j = \sum_{k=1}^{n} \int_{E_k} \{f_x, f_y\} \{\Phi_j, 0\}^{\mathrm{T}}\, \mathrm{d}x\, \mathrm{d}y = \sum_{k=1}^{n} \int_{E_k} f_x \Phi_j\, \mathrm{d}x\, \mathrm{d}y.$$

Then the jth component of the local load vector on E_k is as follows:

- If E_k is an element in the singular zone Ω_S,

$$b_j^{(k)} = \int_{E_k} f_x \Phi_j \, dx \, dy = \int_{\hat{E}_k} \left| J\left(\varphi_{\text{pow}}^2\right) \right| \left(f_x \circ \varphi_{\text{pow}}^2\right) \left(\Phi_j \circ \varphi_{\text{pow}}^2\right) d\hat{x} \, d\hat{y}$$
$$= \int_{\Omega_{\text{st}}^{(*)}} \left| J\left(\Psi_k^S\right) \right| f\left(\Psi_k^S(\xi,\eta)\right) \left(\overline{\mathscr{N}}_j^{(k)}\right) d\xi \, d\eta.$$

- If E_k is an element in the regular zone Ω_S,

$$b_j^{(k)} = \int_{\Omega_{\text{st}}^{(*)}} |J(\Psi_k)| f(\Psi_k(\xi,\eta)) \left(\overline{\mathscr{N}}_j^{(k)}\right) d\xi \, d\eta.$$

In other words, this method uses the conventional finite element method to those elements $\hat{E}_k \in \hat{\Omega}_S$ with the transformed bilinear form, (A.4), and the transformed linear functional, (A.5) (the mapped principal of virtual work), instead of constructing the singular basis functions for the local stiffness matrices and local load vectors for those elements in $E_k \in \Omega_S$. Thus, this method requires virtually no extra cost.

Remark. (1) Instead of PAW in constructing the singular element mappings, we may use the *exponential auxiliary mapping* (EAM) $\varphi_{\text{exp}}^{\beta} : \hat{\Omega}_S \to \Omega_S$ defined by

$$\varphi_{\text{exp}}^{(\beta_1,\beta_2)}(\hat{x},\hat{y}) = (e^{\beta_1 \hat{x}} \cos(\beta_2 \hat{y}), e^{\beta_1 \hat{x}} \sin(\beta_2 \hat{y})). \tag{25}$$

Suppose $\beta_1 = 2, \beta_2 = 0.25$, then we have

$$\left[r^{1/2} \sin(0.15 \log r)\right] \circ \varphi_{\text{exp}}^{(2,0.25)} = e^{\hat{x}} \sin(0.3\hat{y}).$$

The transformed function by EAM is also much smoother than the original function.

(2) In order to destroy the log-type singularity, we can take advantage of the EAM. However, this map transforms a neighborhood Ω_S of the crack tip onto an infinite domain $\hat{\Omega}_S$; hence, the methods (for example, infinite elements introduced in [11,15]) to deal with unbounded domains need to be considered. If either the order of singularity α of the $r^{\alpha} \sin(\varepsilon \log r)$-type singularity is unknown or the oscillating factor ε is large (for example, $\varepsilon > 1$), the EAM is more advantageous than the PAM. However, if the order (intensity) of the singularity is known and the oscillating factor is small, two auxiliary mapping yields almost the same results [11]. It is known that $\alpha = 1/2$ for the crack singularity and the maximum value of the oscillating factor ε for homogeneous bimaterials is 0.17 [26]. Furthermore, it was shown [22] that for most practical orthotropic materials, ε is small. Hence, throughout this paper, we use the PAM.

(3) The number of Gauss points for the numerical results of this paper is 12 for each p-degree. The results in Section 3.3 for the line integral are not necessarily implemented whenever sufficient number of Gauss points are used. For example, the interval of integration is divided into 10 smaller intervals and the Gaussian quadrature is applied with 12 Gauss points on each subinterval. Thus, *implementing the results in the next section to our method is optional.*

3.3. Line integral of singular functions (optional)

The displacement vectors and the stress functions obtained by our method are singular on the singular zone Ω_S. Thus, we have to calculate the line integrals in (16) and (17) with respect to singular functions. In this section, we will show that by change of variables, the line integral of a singular function can be rewritten as a line integral of a smooth function.

Let $\hat{\boldsymbol{u}}$ be the transformed function of $\boldsymbol{u}$ by the power auxiliary mapping φ_{pow}^2 (that is, $\hat{\boldsymbol{u}} = \boldsymbol{u} \circ \varphi_{\text{pow}}^2$). Let $(u_x)_{\text{fe}}$ and $(u_y)_{\text{fe}}$ be FE solutions for the x-displacement and the y-displacement, respectively, that are obtained by our method. Then the displacement functions are singular, however, $(\hat{u}_x)_{\text{fe}}$ and $(\hat{u}_y)_{\text{fe}}$ are smooth functions.

From the standard arguments, with respect to the power auxiliary mapping $\varphi^2_{\mathrm{pow}}(\hat{x},\hat{y})$ of the mapping size 2, we have

$$\begin{aligned} \mathrm{d}x &= \frac{\mathrm{d}x}{\mathrm{d}\hat{x}}\mathrm{d}\hat{x} + \frac{\mathrm{d}x}{\mathrm{d}\hat{y}} = J_{11}\,\mathrm{d}\hat{x} + J_{12}\,\mathrm{d}\hat{y}, \\ \mathrm{d}y &= \frac{\mathrm{d}y}{\mathrm{d}\hat{x}}\mathrm{d}\hat{x} + \frac{\mathrm{d}y}{\mathrm{d}\hat{y}} = J_{21}\,\mathrm{d}\hat{x} + J_{22}\,\mathrm{d}\hat{y}, \end{aligned}$$

where

$$\begin{aligned} J_{11} &= 2\hat{r}\cos\hat{\theta}, \quad J_{12} = 2\hat{r}\sin\hat{\theta}, \\ J_{21} &= -2\hat{r}\sin\hat{\theta}, \quad J_{22} = 2\hat{r}\cos\hat{\theta}. \end{aligned}$$

Furthermore, if we let $\hat{v}(\hat{x},\hat{y}) = v \circ \varphi^2_{\mathrm{pow}}(\hat{x},\hat{y})$, then by chain rule, we have

$$\left\{\frac{\partial v}{\partial x}, \frac{\partial v}{\partial y}\right\}^{\mathrm{T}} = [J_{ij}]^{-1} \cdot \left\{\frac{\partial \hat{v}}{\partial \hat{x}}, \frac{\partial \hat{v}}{\partial \hat{y}}\right\}^{\mathrm{T}}, \tag{26}$$

where

$$[J_{ij}]^{-1} = \frac{1}{2\hat{r}}\begin{bmatrix} \cos\hat{\theta} & -\sin\hat{\theta} \\ \sin\hat{\theta} & \cos\hat{\theta} \end{bmatrix}. \tag{27}$$

Let $[E_{ij}]$ be a 3×3 symmetric positive definite matrix of material constants in the stress–strain relation $\{\sigma^{(u)}\} = [E_{ij}]\{\varepsilon^{(u)}\}$. Then, we have the following lemma showing that the line integrals for the energy release rates can be calculated by a line integral of a smooth function.

Lemma 3.1.

$$\begin{aligned} \int_0^{\Delta} \sigma_y(x,0)u_y(\Delta - x,\pi)\,\mathrm{d}x = \frac{\pi}{4}\int_{-1}^{1} &\left[F\left(\frac{\partial \hat{u}_x}{\partial \hat{x}}, \frac{\partial \hat{u}_x}{\partial \hat{y}}, \frac{\partial \hat{u}_y}{\partial \hat{x}}, \frac{\partial \hat{u}_y}{\partial \hat{y}}\right)(\sqrt{\Delta}\sin T, 0)\right] \\ &\times \left[\hat{u}_y(0, \sqrt{\Delta}\cos T)\right][\sqrt{\Delta}\cos T]\,\mathrm{d}\xi, \end{aligned}$$

where $T = (\pi/4)(\xi + 1)$ *and*

$$\begin{aligned} F\left(\frac{\partial \hat{u}_x}{\partial \hat{x}}, \frac{\partial \hat{u}_x}{\partial \hat{y}}, \frac{\partial \hat{u}_y}{\partial \hat{x}}, \frac{\partial \hat{u}_y}{\partial \hat{y}}\right) := \Bigg[&(E_{21}\cos\hat{\theta} + E_{23}\sin\hat{\theta})\frac{\partial \hat{u}_x}{\partial \hat{x}} + (-E_{21}\sin\hat{\theta} + E_{23}\cos\hat{\theta})\frac{\partial \hat{u}_x}{\partial \hat{y}} \\ &+ (E_{22}\sin\hat{\theta} + E_{23}\cos\hat{\theta})\frac{\partial \hat{u}_y}{\partial \hat{x}} + (E_{22}\cos\hat{\theta} - E_{23}\sin\hat{\theta})\frac{\partial \hat{u}_y}{\partial \hat{y}}\Bigg]. \end{aligned} \tag{28}$$

Proof. From (26) and the stress–strain relation, we have

$$\hat{\sigma}_y(\hat{x},\hat{y}) = \frac{1}{2\hat{r}}F\left(\frac{\partial \hat{u}_x}{\partial \hat{x}}, \frac{\partial \hat{u}_x}{\partial \hat{y}}, \frac{\partial \hat{u}_y}{\partial \hat{x}}, \frac{\partial \hat{u}_y}{\partial \hat{y}}\right)(\hat{x},\hat{y}), \tag{29}$$

where $F(\cdot,\cdot,\cdot,\cdot)$ is defined by (28). Since $\mathrm{d}\hat{y} = 0$ along the $\hat{x}$-axis,

$$\mathrm{d}s = \sqrt{\mathrm{d}x^2 + \mathrm{d}y^2} = \sqrt{(J_{11}\mathrm{d}\hat{x})^2 + (J_{12}\mathrm{d}\hat{x})^2} = 2\hat{r}\mathrm{d}\hat{x} \tag{30}$$

along $\hat{\theta} = 0$.

Let g be a function defined by $g(x,y) = (\Delta - x, y)$. Then

$$\begin{aligned} u_y \circ g \circ \varphi^2_{\mathrm{pow}}(\hat{r},\hat{\theta}) &= u_y \circ \varphi^2_{\mathrm{pow}} \circ \left(\varphi^2_{\mathrm{pow}}\right)^{-1} \circ g \circ \varphi^2_{\mathrm{pow}}(\hat{r},\hat{\theta}) \\ &= u_y \circ \varphi^2_{\mathrm{pow}} \circ \left(\varphi^2_{\mathrm{pow}}\right)^{-1} \circ g \circ (\hat{r}^2, 2\hat{\theta}) \\ &= \hat{u}_y \circ \left(\varphi^2_{\mathrm{pow}}\right)^{-1} (\Delta - \hat{r}^2, 2\hat{\theta}) \\ &= \hat{u}_y(\sqrt{\Delta - \hat{r}^2}, \hat{\theta}). \end{aligned} \tag{31}$$

And also note that through the auxiliary mapping φ^2_{pow}, the lines $\theta = \pi$ and $\theta = -\pi$ are mapped to the line $\hat{\theta} = \pi/2$ and $\hat{\theta} = -\pi/2$, respectively, in the $\hat{x}$–$\hat{y}$ plane.

Then from (28)–(31), we have

$$\begin{aligned} \int_0^{\Delta} \sigma_y(x,0)u_y(\Delta - r, \pi)\,\mathrm{d}s &= \int_0^{\Delta} \sigma_y(x,0)u_y \circ g(r,\pi)\,\mathrm{d}s \\ &= \int_0^{\sqrt{\Delta}} \left[\sigma_y \circ \varphi^2_{\mathrm{pow}}(\hat{x},0)\right]\left[u_y \circ g \circ \varphi^2_{\mathrm{pow}}(\hat{x},\pi/2)\right] 2\hat{r}\,\mathrm{d}\hat{x} \\ &= \int_0^{\sqrt{\Delta}} \hat{\sigma}_y(\hat{x},0)\hat{u}_y(\sqrt{\Delta - \hat{x}^2}, \pi/2) 2\hat{r}\,\mathrm{d}\hat{x} \\ &= \int_0^{\sqrt{\Delta}} F\left(\frac{\partial \hat{u}_x}{\partial \hat{x}}, \frac{\partial \hat{u}_x}{\partial \hat{y}}, \frac{\partial \hat{u}_y}{\partial \hat{x}}, \frac{\partial \hat{u}_y}{\partial \hat{y}}\right)(\hat{x},0)\hat{u}_y(\sqrt{\Delta - \hat{x}^2}, \pi/2)\,\mathrm{d}\hat{x} \\ &= \int_0^{\sqrt{\Delta}} F\left(\frac{\partial \hat{u}_x}{\partial \hat{x}}, \frac{\partial \hat{u}_x}{\partial \hat{y}}, \frac{\partial \hat{u}_y}{\partial \hat{x}}, \frac{\partial \hat{u}_y}{\partial \hat{y}}\right)(\hat{x},0)\hat{u}_y(0, \sqrt{\Delta - \hat{x}^2})\,\mathrm{d}\hat{x}. \end{aligned} \tag{32}$$

By the substitution $\hat{x} = \sqrt{\Delta}\sin t$, the forgoing line integral becomes

$$\int_0^{\pi/2} \left[F\left(\frac{\partial \hat{u}_x}{\partial \hat{x}}, \frac{\partial \hat{u}_x}{\partial \hat{y}}, \frac{\partial \hat{u}_y}{\partial \hat{x}}, \frac{\partial \hat{u}_y}{\partial \hat{y}}\right)(\sqrt{\Delta}\sin t, 0)\right]\left[\hat{u}_y(0, \sqrt{\Delta}\cos t)\right][\sqrt{\Delta}\cos t]\,\mathrm{d}t.$$

By the substitution $t = (\pi/4)(\xi + 1)$, we have the lemma. □

For the line integral, $\hat{u}_y$ is evaluated along the straight side $S_2^{(4)} \equiv \overline{6 \to 1}$ of the curved triangular element $\hat{E}_4 \equiv \overline{5 \to 6 \to 1}$ of $\hat{\Omega}_{\mathrm{S}}$ (see Fig. 1) and $\partial\hat{u}_x/\partial\hat{x}$, $\partial\hat{u}_x/\partial\hat{y}$, $\partial\hat{u}_y/\partial\hat{x}$, $\partial\hat{u}_y/\partial\hat{y}$ are evaluated along the straight side $S_3^{(1)} \equiv \overline{1 \to 2}$ of the curved triangular element $\hat{E}_1 \equiv \overline{2 \to 3 \to 1}$ of $\hat{\Omega}_{\mathrm{S}}$ (see Fig. 1).

The FE approximations of $\hat{u}_x$ and $\hat{u}_y$ can be expressed of the form

$$\sum_{l=1}^{m_k} a_l(\phi_l \circ (\hat{\boldsymbol{\Psi}}_k)^{-1})(\hat{x},\hat{y}),$$

where ϕ_l is a polynomial basis function in the reference element $\Omega^{(\mathrm{t})}_{\mathrm{st}}$. Generally, the elemental mapping $\hat{\boldsymbol{\Psi}}_k$ of blending type is a rational function (see A.6). However, it will be shown in the following lemma that the integrand of the transformed line integral in Lemma 3.1 is polynomial function.

From now on, by abusing notations, the FE approximations of $\hat{u}_x$ and $\hat{u}_y$ will be denoted by $\hat{u}_x$ and $\hat{u}_y$, respectively.

Lemma 3.2. *The elemental mapping of blending type defined by* (A.6) *is linear on the second and the third sides of the reference triangular element. Hence the finite element solutions $\hat{u}_x$ and $\hat{u}_y$ of displacement functions are polynomial functions along these sides.*

Proof. Consider the elemental mapping, $\hat{\boldsymbol{\Psi}}_1$, of blending type from the reference triangular element to a transformed element $\hat{E}_1$:

$$\hat{\boldsymbol{\Psi}}_1 : \Omega_{\mathrm{st}}^{(\mathrm{t})} = \Delta V_1^{(\mathrm{t})} V_2^{(\mathrm{t})} V_3^{(\mathrm{t})} \to \hat{E}_1 = \Delta \hat{V}_1 \hat{V}_2 \hat{V}_3 \subset \hat{\Omega}_{\mathrm{S}}. \tag{33}$$

In the definition of the blending mapping (A.6), the term, $4L_1L_2$, is vanishing along the side $S_2^{(\mathrm{st})} \equiv \overline{V_2^{(\mathrm{t})} \to V_3^{(\mathrm{t})}}$ and the side $S_3^{(\mathrm{st})} \equiv \overline{V_3^{(\mathrm{t})} \to V_1^{(\mathrm{t})}}$ of $\Omega_{\mathrm{st}}^{(\mathrm{t})}$. Therefore, along the sides $S_2^{(\mathrm{st})}$ and $S_3^{(\mathrm{st})}$, the elemental mapping $\hat{\boldsymbol{\Psi}}_1$ becomes linear

$$\hat{\boldsymbol{\Psi}}_1(\hat{x}, \hat{y}) = [\hat{V}_1 L_1 + \hat{V}_2 L_2 + \hat{V}_3 L_3](\hat{x}, \hat{y}),$$

where L_1, L_2, L_3 are the standard linear basis functions (see Appendix A.1.3). Similarly, the element mapping $\hat{\boldsymbol{\Psi}}_4 : \Omega_{\mathrm{st}}^{(\mathrm{t})} \to \hat{E}_4 \subset \hat{\Omega}_{\mathrm{S}}$ (Fig. 1) is also linear along the sides $S_2^{(\mathrm{st})}$ and $S_3^{(\mathrm{st})}$. Thus, for this line integral, $(\hat{\boldsymbol{\Psi}}_1)^{-1}$ and $(\hat{\boldsymbol{\Psi}}_4)^{-1}$ are linear and hence $\phi_l \circ (\hat{\boldsymbol{\Psi}}_k)^{-1}(\hat{x}, \hat{y})$, $k = 1, 4$ are polynomials. Here ϕ_l stands for a polynomial basis function in $\Omega_{\mathrm{st}}^{(\mathrm{t})}$. □

4. The energy release rates for interlaminar cracks between two weakly dissimilar materials

Throughout this paper, E and v denote the modulus of elasticity and Poisson's ratio, respectively. $\lambda = Ev/((1+v)(1-2v))$ and $\mu = E/(2(1+v))$ are Lame's constants.

Let us consider an interface crack of a bimaterial plate that consists of material 1 with elastic constants μ_1 and v_1 and material 2 with elastic constants μ_2 and v_2. Then the oscillating factor, which represents the order of discontinuity of the two materials, is given by

$$\varepsilon = \frac{1}{2\pi} \ln \left[\frac{\mu_1 + \mu_2 \kappa_1}{\mu_2 + \mu_1 \kappa_2} \right], \tag{34}$$

where for $i = 1, 2$, $\kappa_i = 3 - 4v_i$ for plane strain, $\kappa_i = (3 - v_i)/(1 + v_i)$ for plane stress.

Without loss of generality, ε may be assumed to be positive and it is zero for a homogeneous plate. Moreover, it takes the maximum value $\ln 3/(2\pi) = 0.17485$ when $v_1 = 0$ and $\mu_2 = \infty$. Due to their oscillatory nature, the mode-separated energy release rates for interface cracks of bimaterials do not converge as $\Delta \to 0$, in general.

Suppose a fiber-reinforced material is a laminate whose layers are of the same material and may have different fiber orientation. Then it can be proved by using similar arguments to those in [16,24,25] that the oscillating factors of interlaminar cracks of such laminates are expected to be very small. In other words, the mode-separated energy release rates (16) and (17) for such fiber-reinforced materials are virtually constant when

$$10^{-9} \leqslant \frac{\Delta}{h} \leqslant 10^{-1},$$

where h denotes the thickness of layers. Moreover, if $\frac{\Delta}{h} \leqslant 10^{-9}$, then Δ is smaller than the diameter of the fiber; hence, the Δ-neighborhood of the crack tip does not contain any fiber, unless we are concerned with

the nano-technology. In other words, the Δ-neighborhood of a crack consists of a homogeneous material (resin only); hence, we may claim that $\varepsilon = 0$ whenever $\Delta/h \leqslant 10^{-9}$. In Section 5, we will confirm the following:

- The mode-separated energy release rates for the cracks of a laminate virtually converge when its layers are of the same material and may have different fiber orientations (Tests (A) and (B) of Example 5.4). However, those results presented in [2] are different from this result.

5. Computational results

In this section, we will apply our method to compute energy release rates for

$$\begin{cases} (1) & \text{cracks in homogeneous isotropic materials,} \\ (2) & \text{cracks in isotropic bimaterials,} \\ (3) & \text{interlaminar cracks of fiber-reinforced orthotropic materials.} \end{cases}$$

5.1. Cracks in homogeneous materials

Since the displacement functions near crack tip of homogeneous isotropic materials are non-oscillating singular functions, the mode-separated energy release rates converge. In this section, the mapping method (MAM) in the framework of the *p*-FEM yields better results than the conventional method that use quarter-point singularity elements in the framework of the *h*-FEM.

It is known that the Mode I energy release rate is expressed in terms of the stress intensity factor K_{I} as follows:

$$\begin{cases} G_{\mathrm{I}} = \frac{K_{\mathrm{I}}^2}{E} & \text{for plane stress,} \\ G_{\mathrm{I}} = \frac{(1-\nu^2)K_{\mathrm{I}}^2}{E} & \text{for plane strain,} \end{cases} \tag{35}$$

where ν and E are Poisson's ratio and Young's modulus, respectively. The expression of G_{II} in terms of K_{II} is similar. In this section, we assume that $\nu = 0.3, E = 10^6$ and the computations are for plain strain. $\mathscr{U}(u_{\mathrm{fe}})$ denotes the strain energy of u_{fe}.

Example 5.1. *Center-cracked tension specimen*: We consider a center-cracked plate $[-b, b] \times [-k, k]$ with crack length $2a$ under uniform tension S as shown in Fig. 2(a). Then by Appendix 2.1 of [6], the mode *I* stress intensity factor is

$$K_{\mathrm{I}} = S\sqrt{\pi a}\{1.0 + 0.128(a/b) - 0.288(a/b)^2 + 1.523(a/b)^3\}, \tag{36}$$

when $0 < a/b < 0.7$.

In the first example, we choose $S = 100$, $b = 1.0, a = 0.8, k = 2$. Then by Eqs. (35) and (36), we obtain $G_{\mathrm{I}} = 0.0754556$.

From the symmetries in the problem, only one-quarter of the specimen was analyzed. Fig. 2(c) is a mesh for *p*-FEM which consists of four triangular elements and 15 quadrilateral elements. For a neighborhood Ω_{S} of the crack (the mapping zone) for our method, we select the inner most four triangular elements and

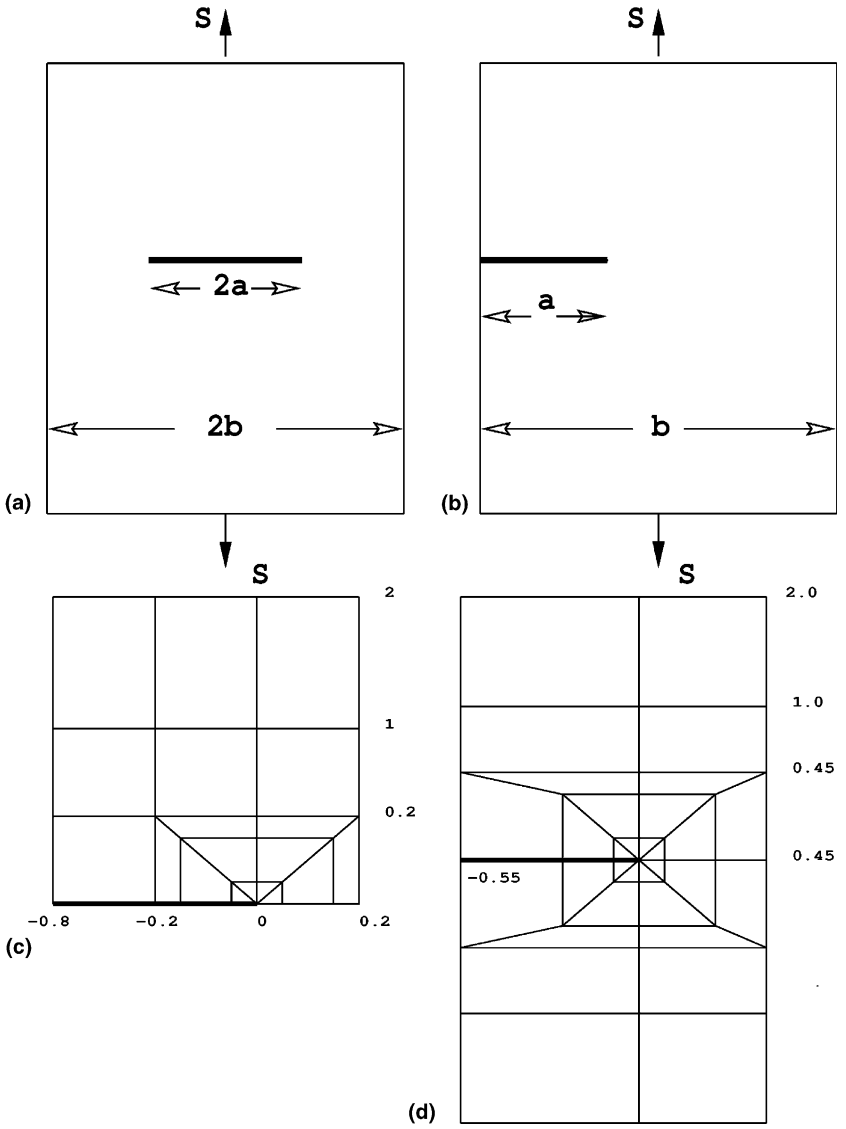

Fig. 2. Schemes of (a) center-cracked tension (CCT) specimen, (b) single edge-notched (SEN) specimen, (c) finite element mesh of one-quarter of CCT specimen, (d) finite element mesh of SEN specimen.

the four quadrilateral elements surrounding the triangular elements. This specimen is analyzed in the following aspects:

- The mode I energy release rate G_{I} by our method.
- The mode I energy release rate $G_{(\mathrm{I})}$ by the conventional p-FEM without using our method (that is, the mapping size of the auxiliary mapping defined by (19) is $\beta = 1$).
- The total energy release rate by applying central difference approximation to the strain energy computed by our method.
- The convergence of total strain energy computed by our method.

We have observed the followings:

(1) Table 1 shows that the relative error of the best $G_{\mathrm{I}}(p=9)$ is 0.02%. Nevertheless, the best G_{I} in [17] (obtained by using cubic singularity elements) has 0.3% in the relative error.
(2) By comparing G_{I} and $G_{(\mathrm{I})}$ from Table 1, one can see the superiority of our method over the conventional p-FEM (that is, 0.02% versus 11% in relative error when $p=9$).

Relative errors in percent of the total strain energy (which indicates the error of FE solutions, section 4.2 of [23]), $G_{\mathrm{I}}, G_{(\mathrm{I})}$, and $G_{\mathrm{total}} = G_{\mathrm{I}} + G_{\mathrm{II}}$ are depicted in Fig. 3.

Example 5.2 (*Single edge-notched specimen* (SENS)). The second example is single edge-notched plate $[-a, b-a] \times [-k, k]$ under uniform tension S as Fig. 2(b). It is known [6] that the mode I stress intensity factor for single edge-notched plate is

$$K_{\mathrm{I}} = S\sqrt{\pi a}\{1.12 - 0.23(a/b) + 10.55(a/b)^2 - 21.72(a/b)^3 + 30.39(a/b)^4\}, \tag{37}$$

whenever $0 < a/b < 0.7$.

Table 1
Computation of one-fourth of center-cracked plate $[-b, b] \times [-k, k]$ with crack length $2a$ under uniform tension $S = 100$, where in this computation $b = 1.0,\ a = 0.8,\ k = 2,\ E = 10^6$. G_{I} and $G_{(\mathrm{I})}$ are the mode I energy release rates obtained by the new method and by the conventional p-FEM, respectively. G_{total} is computed by the central difference approximation (14) with $\Delta = 0.5 \times 10^{-8}$. The row "$\infty$" indicates the exact values

p	DOF	$\mathscr{U}(u_{\mathrm{FE}})E/4$	G_{I}	$G_{(\mathrm{I})}$	G_{total}
1	52	15237.9432999	0.0953976	0.0320149	0.0534118
2	140	16988.7410759	0.0643846	0.0561566	0.0738187
3	236	17078.9934190	0.0719215	0.0577928	0.0753140
4	370	17109.7839910	0.0745717	0.0595203	0.0754432
5	542	17119.5240645	0.0751520	0.0616602	0.0754757
6	752	17121.9398467	0.0752964	0.0633685	0.0754742
7	1000	17122.5523856	0.0753812	0.0648338	0.0754758
8	1286	17122.6845944	0.0754230	0.0660116	0.0754776
9	1610	17122.7069546	0.0754441	0.0669814	0.0754783
∞	∞	17122.7105178	0.0754556	0.0754556	0.0754782

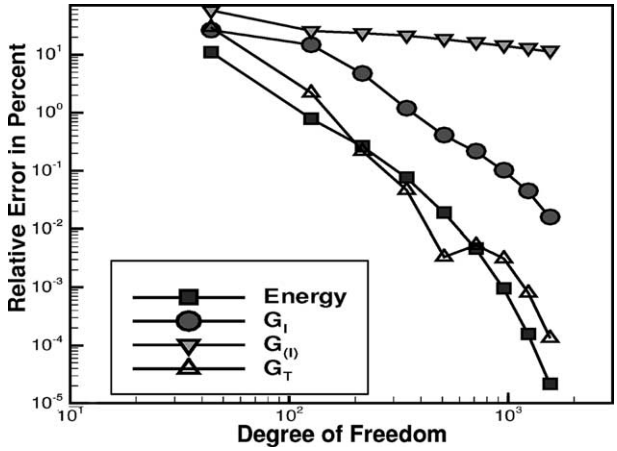

Fig. 3. Relative error (%) of "Energy" (total strain energy), $G_{\mathrm{I}},\ G_{(\mathrm{I})}$ (Mode I energy release rate without applying the new method), G_{total} of CCT specimen.

In this example, we use the crack length $a = 0.55$ and $b = 1.0, k = 2.0$, and the remote uniform traction load is $S = 100$. Then by Eqs. (35) and (37), we obtain $K_I = 440.6271928$ and $G_I = (1 - \nu^2)K_I^2/E = 0.176678$.

Fig. 2(d) is a finite element mesh for our method which consists of eight triangular elements and 28 quadrilateral elements. For the mapping zone Ω_S (the neighborhood of the crack tip) for our method, we select the inner most eight triangular elements and the inner most eight quadrilateral elements surrounding the triangular elements. The SENS was analyzed in the same ways as the previous example. The results are displayed in Table 2, from which we have the following conclusions:

(1) Table 2 shows that the relative error of G_I is 0.6% when $p = 9$. However, the best G_I in [17] (obtained by using cubic singularity elements) has 3.3% in the relative error.
(2) By comparing G_I and $G_{(I)}$ from Table 2, once again, one can see the superiority of the mapping method over the conventional p-method (i.e., 0.6% versus 11.8% in relative error when $p = 9$).

Relative errors in percent of the total energy, G_I (obtained by using our method), $G_{(I)}$ (obtained without using our method), and G_{total} are depicted in Fig. 4.

5.2. Interfacial cracks between isotropic layers

In this section, we consider an interface crack of a bimaterial plate that consists of material 1 with elastic constants μ_1 and ν_1 and material 2 with elastic constants μ_2 and ν_2. Then, it is known that the mode-separated energy release rates for interface cracks of bimaterials do not converge as $\Delta \to 0$. In fact, if the oscillating factor ε is not very small, G_I is increasing (decreasing) while G_{II} is decreasing (increasing), respectively, as $\Delta \to 0$.

Example 5.3 (*Isotropic bimaterial plate*). Let us consider a bimaterial of epoxy and glass [10] shown in Fig. 5 such that the material properties are as follows:

$$\begin{aligned} &E_1 = 1.72 \text{ Gpa}, \quad \nu_1 = 0.4 \text{ (epoxy)},\\ &E_2 = 68.95 \text{ Gpa}, \quad \nu_2 = 0.2 \text{ (glass)}. \end{aligned} \tag{38}$$

Then from (34), $\varepsilon = 0.0486476$.

Table 2
Plain strain computation for single edge-notched plate$[-a, b-a] \times [-2, 2]$ under uniform tension $S = 100$, where $a = 0.55$ is the crack length, $b = 1.0$, and $E = 10^6$. G_I and $G_{(I)}$ are the mode I energy release rates obtained by the new method and the conventional p-FEM, respectively. G_{total} is computed by the central difference approximation (14) with $\Delta = 0.5 \times 10^{-8}$. The row "$\infty$" indicates the exact values

p	DOF	$\mathscr{U}(u_{FE})E$	G_I	$G_{(I)}$	G_{total}
1	80	31156.9824930	0.1502874	0.0555432	0.0979730
2	222	38163.5473336	0.1501532	0.1270484	0.1648749
3	380	38628.4771876	0.1579704	0.1283439	0.1702329
4	602	39122.5168253	0.1721155	0.1378598	0.1747564
5	888	39189.0227303	0.1750825	0.1432396	0.1756045
6	1238	39197.2704305	0.1754222	0.1473620	0.1756870
7	1652	39198.3009764	0.1754423	0.1507687	0.1757009
8	2130	39198.4857040	0.1755709	0.1535316	0.1757021
9	2672	39198.5111936	0.1756254	0.1558046	0.1757029
∞	∞	39198.5156205	0.1766780	0.1766780	0.1766780

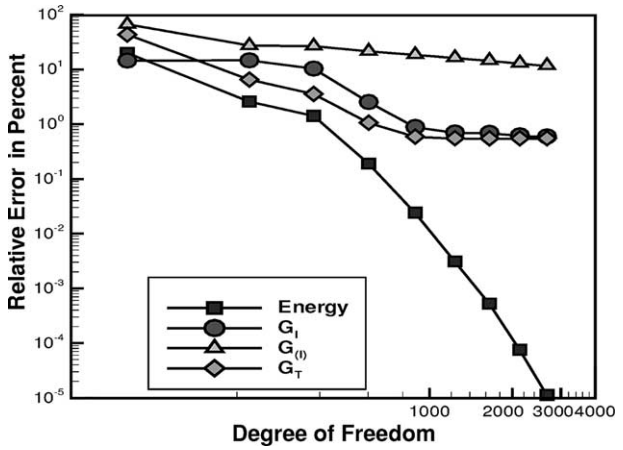

Fig. 4. Relative error (%) of "Energy" (total strain energy), G_{I}, $G_{(\mathrm{I})}$ (Mode I energy release rate without applying the new method), G_{total} of SEN specimen.

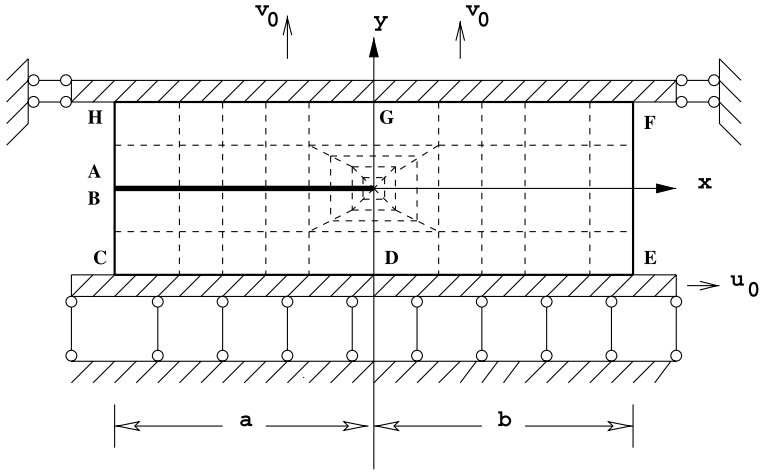

Fig. 5. Scheme of the isotropic bimaterial and finite element mesh (dotted lines).

In this example, the sizes of a bimaterial specimen are chosen as follows: the crack length is $a = 0.75$ dm, $a = b$, $u_0 = 0$, $v_0 = 6.65$ μm, and the layer thickness are $h_1 = h_2 = 0.1$ dm. The mesh for finite element analysis of this problem is shown as the dotted lines in Fig. 5. We assume the load vector $\{f\} = \{0, 0\}^{\mathrm{T}}$ and the boundary conditions are assigned as follows: $\{u\} = \{0, 0\}^{\mathrm{T}}$ along the side $\overline{CDE}$ (Fig. 5); $\{u\} = \{0, v_0\}^{\mathrm{T}}$ along the side $\overline{FGH}$; free along all the other parts of boundaries.

From Fig. 6, one can see that G_{I} is decreasing and G_{II} is increasing as $\Delta \to 0$. In general, the smaller the oscillating factor ε is, the flatter the curve drawn in Δ versus $G_{\mathrm{I}}/G_{\mathrm{total}}$ (see [26]). Moreover, it was shown in [26] that the graphs of $G_{\mathrm{I}}/G_{\mathrm{total}}$ and $G_{\mathrm{II}}/G_{\mathrm{total}}$ with respect to Δ are straight lines with small slopes when the oscillating factor ε is 0.001.

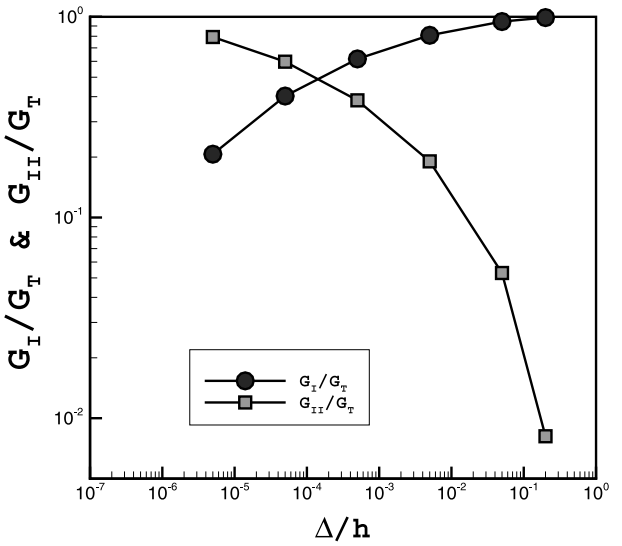

Fig. 6. Finite element analysis of G_I and G_{II} for isotropic bimaterial when the oscillating factor $\varepsilon = 0.0486$.

5.3. Interfacial cracks between orthotropic layers

In Section 5.2, we showed that the mode-separated energy rates for interface cracks for isotropic bimaterials do not converge.

In this section, we consider the interlaminar cracks of laminates of fiber-reinforced layers. If layers are of the same material and its fiber directions are different, the oscillating factor ε (the order of discontinuity between layers) expected to be very small.

For various tests of interlaminar cracks of laminates that consist of fiber-reinforced layers with various fiber angles, G_I and G_{II} are virtually constant when $10^{-9} < \Delta/h < 10^{-1}$, where h is the thickness of the layers. Moreover, if $\Delta/h < 10^{-9}$, then the crack tip is well inside the homogeneous materials(resin). In other words, in fiber-reinforced composite materials, if Δ is very small, then physics of the Δ-neighborhood of the material is changed from orthotropic (fiber and resin) to isotropic (resin only). Hence, the oscillating factor ε is 0 for such case (see Table 3).

In order to compare the results obtained by our method with the results reported in [2], the engineering properties of ply with unidirectional fiber used in examples of this subsection are the same as those in [2].

Table 3
G_I and G_{II} for interface crack of isotropic bimaterial

Δ/h	G_I	G_I	G_{II}	G_{II}
	$p = 6$	$p = 8$	$p = 6$	$p = 8$
1.0E − 1	0.0426679	0.0428116	0.0011769	0.0011675
5.0E − 2	0.0415825	0.0416705	0.0023384	0.0023284
5.0E − 3	0.0355615	0.0356307	0.0084044	0.0083841
5.0E − 4	0.0270981	0.027147	0.0169095	0.0168826
5.0E − 5	0.0177138	0.0177394	0.0263338	0.0262994
5.0E − 6	0.0090767	0.0090939	0.0349806	0.0349481
1.0E − 6	0.0043625	0.0043484	0.0398225	0.0397115

That is, the material properties of carbon–epoxy ply used in the numerical tests in Examples 5.4(A) and (B) are the following:

$$E_{11} = 134.45 \text{ Gpa}, \quad E_{22} = E_{33} = 10.20 \text{ Gpa},$$
$$G_{12} = G_{13} = 5.52 \text{ Gpa}, \quad G_{23} = 3.43 \text{ Gpa},$$
$$v_{12} = v_{13} = 0.30, \quad v_{23} = 0.49.$$

Example 5.4. (A). The first laminate specimen [0/90/0] consists of plane strain drop-ply configuration of 0° and 90° graphite–epoxy plies as shown in Fig. 7(a), which is Test #1 of [2]. In this example, the thickness h of the layer next to the interlaminar crack is 0.125, the crack length is 0.4, and Δ denotes the side length of the inner most eight triangular element (Fig. 8). The singular zone Ω_S for our method is the 40 elements inside the square neighborhood $[-0.125, 0.125] \times [-0.125, 0.125]$ of the crack tip.

Our method is applied to estimate G_I and G_{II} when Δ/h is $10^{-1}, \ldots, 10^{-7}$. Table 4 depicts the results when the degree of basis functions are 4, 8, and 9. The results in Table 4 show that the energy release rate is virtually Δ-independent whenever the p-degree of basis functions is 8 or 9 (FE solutions for stress functions become highly accurate).

On the other hand, if p-degree is $\leqslant 4$, G_I is increasing and G_{II} is decreasing as $\Delta \to 0$. This is a similar pattern as those reported in [12]. In order to compare the figures reported in [2], G_{II}/G_I versus Δ/h are plotted in Fig. 9. The results when $p = 4$ is similar to those in [2].

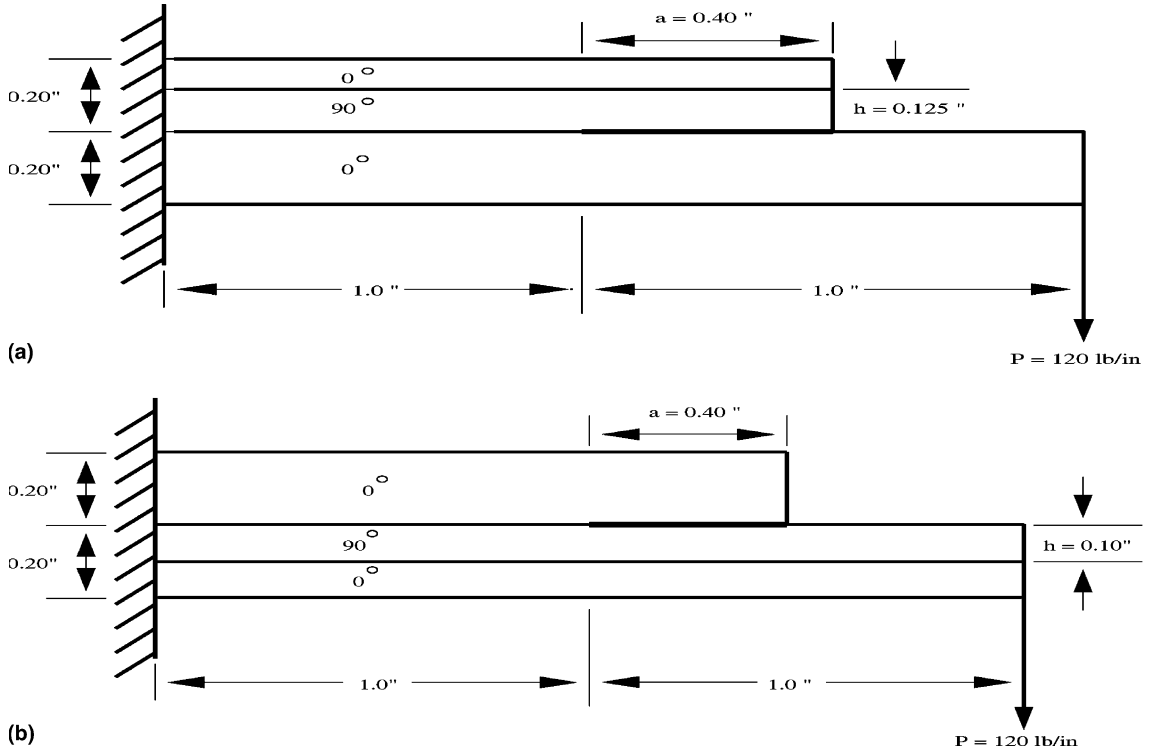

Fig. 7. Scheme of drop-ply configuration for the test problems (A) and (B) of Example 5.4.

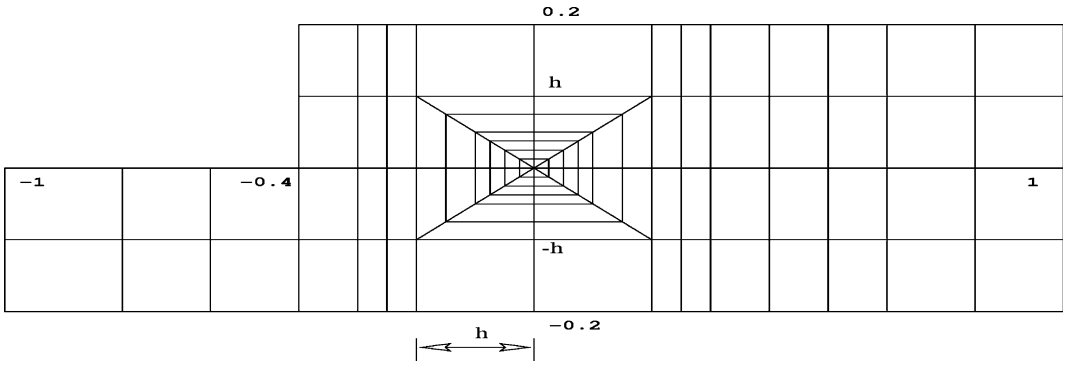

Fig. 8. Mesh for the finite element analysis for the problems 5(A) and 5(B).

Table 4
G_I and G_{II} for the interlaminar crack of drop-ply configuration which is Test #1 of [2] (see Fig. 7(a))

Δ/h	G_I			G_{II}		
	$p=4$	$p=8$	$p=9$	$p=4$	$p=8$	$p=9$
1.0E−1	2.676E−2	2.723E−2	2.725E−2	0.361E−2	0.396E−2	0.396E−2
1.0E−2	2.678E−2	2.725E−2	2.727E−2	0.359E−2	0.395E−2	0.394E−2
1.0E−3	2.676E−2	2.725E−2	2.727E−2	0.359E−2	0.395E−2	0.394E−2
1.0E−4	2.672E−2	2.725E−2	2.727E−2	0.359E−2	0.395E−2	0.394E−2
1.0E−5	2.646E−2	2.725E−2	2.727E−2	0.377E−2	0.395E−2	0.394E−2
1.0E−6	3.874E−2	2.726E−2	2.727E−2	0.172E−2	0.396E−2	0.394E−2
1.0E−7	3.272E−2	2.726E−2	2.727E−2	0.232E−2	0.396E−2	0.394E−2

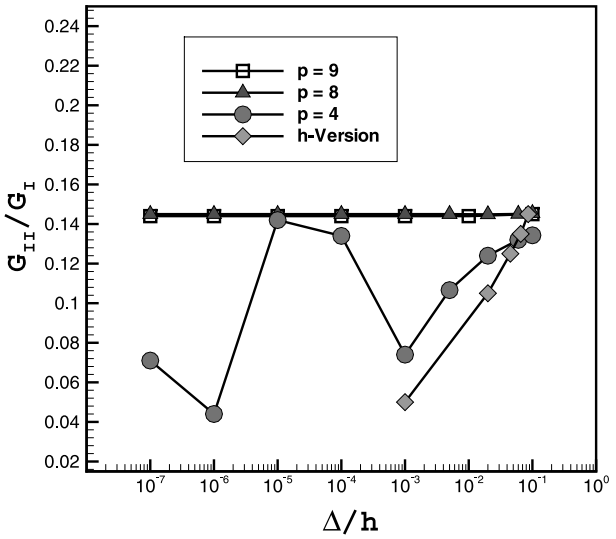

Fig. 9. Results of the p-version finite element analysis of laminate $[0/90/0]$ with $h = 0.125$ (Fig. 7(a)).

The computation costs are comparable. In this p-version finite element analysis, 90 quadrilateral elements and eight triangular elements are used as it is shown in Fig. 8. On the other hand, in [2], 763 eight-noded quadrilateral interpolation elements are used for the finite element analysis of this test problem. In [2], the singular and non-singular near-tip meshes consist of 18 rings of elements meshed over a length equal to $h/2$. However, Fig. 8 shows that the near-tip meshes of our method consist of five rings of elements over $[-h,h]\times[-h,h]$ near the crack tip, $h=0.125$.

Actually, the mapping technique in p-FEM does not require such a very fine mesh as shown in Fig. 8. If we put only two rings with side length, for example, $r_1=h/10, r_2=h/2$, then the number of elements is reduced from 98 to 74 and the mapping zone for the mapping method consists of eight quadrilateral elements and eight triangular elements. The accuracy of the finite element solution obtained by 74 elements mesh (two rings mesh) is virtually the same as that obtained by the 98 elements mesh (five rings mesh). The reason to put five rings in Fig. 8 is to apply the definition (Eq. (14)) of total energy release rate when Δ is extremely small.

(B). Consider a laminate $[0/0/90/0]$ as shown in Fig. 7(b), in which $h=0.1$. The energy release rates of this case are much higher than those of Example 5.4(A) and the mode mix for Examples 5.4 (A) and (B) are different as it is pointed out in [2]. This is Test #2 of [2].

As shown in Table 5, the mode-separated energy release rates also virtually converge whenever p-degree is 8, 9. $G_{\mathrm{II}}/G_{\mathrm{I}}$ is depicted in Fig. 10 with respect to $\Delta/h=10^{-n}, n=1,\ldots,7$. Once again, Fig. 10 shows that $G_{\mathrm{II}}/G_{\mathrm{I}}$ when $p=4$ is similar to those in [2].

(C). Finally, we consider the interlaminar crack between two layers which are highly dissimilar. For instance, consider Example 5.4(A) (Fig. 7(a)) when the first layer and the second layer are the graphite-epoxy composites and the third layer of 0° fiber orientation is a graphite–polymer composite with the following material properties (Table 2.1 of [8]):

$$E_{11}=155\ \text{Gpa},\quad E_{22}=E_{33}=12.10\ \text{Gpa},$$
$$G_{12}=G_{13}=3.20\ \text{Gpa},\quad G_{23}=4.40\ \text{Gpa},$$
$$v_{12}=v_{13}=0.248,\quad v_{23}=0.458.$$

In this case, the degree of mismatch of two layers is large and hence the oscillating factor cannot be negligible. Thus, as shown in Fig. 11, the mode-separated energy release rates do not converge.

From Examples 5.4(A)–(C), we have the following observations:

- Actually, in cases (A) and (B), since two layers are weakly mismatched, the oscillating factors ε become small. Therefore, the energy release rates for the Mode I and the Mode II virtually converge. In practical fiber-reinforced composite materials, the layers are orthotropic materials which are the composition of one resin and one fibre materials, but may have different fiber orientations. In other words, any

Table 5
G_{I} and G_{II} for the interlaminar crack of drop-ply configuration which is Test #2 of [2] (see Fig. 7(b))

Δ/h	G_{I}			G_{II}		
	$p=4$	$p=8$	$p=9$	$p=4$	$p=8$	$p=9$
1.0E−1	3.310E−2	3.260E−2	3.262E−2	8.526E−2	8.145E−2	8.125E−2
1.0E−2	3.286E−2	3.252E−2	3.254E−2	8.524E−2	8.153E−2	8.133E−2
1.0E−3	3.277E−2	3.252E−2	3.254E−2	8.526E−2	8.152E−2	8.133E−2
1.0E−4	3.306E−2	3.252E−2	3.254E−2	8.647E−2	8.153E−2	8.133E−2
1.0E−5	3.275E−2	3.252E−2	3.254E−2	8.719E−2	8.151E−2	8.132E−2
1.0E−6	2.816E−2	3.252E−2	3.254E−2	8.351E−2	8.154E−2	8.135E−2
1.0E−7	2.990E−2	3.255E−2	3.255E−2	9.343E−2	8.136E−2	8.129E−2

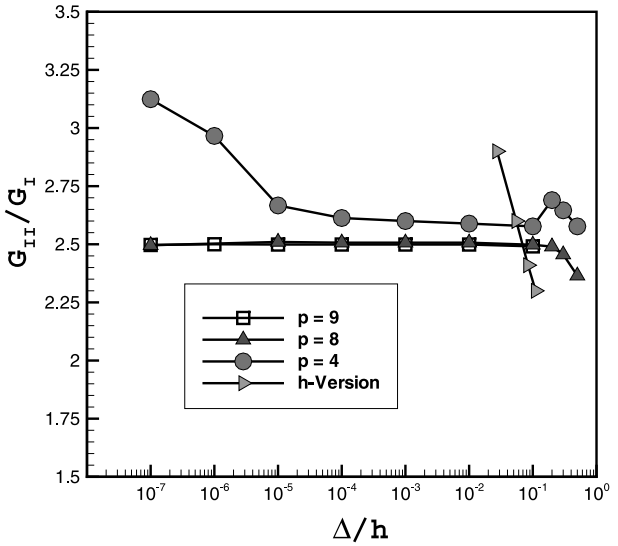

Fig. 10. Results of the p-version finite element analysis of laminate $[0/0/90/0]$ with $h = 0.1$ (Fig. 7(b)).

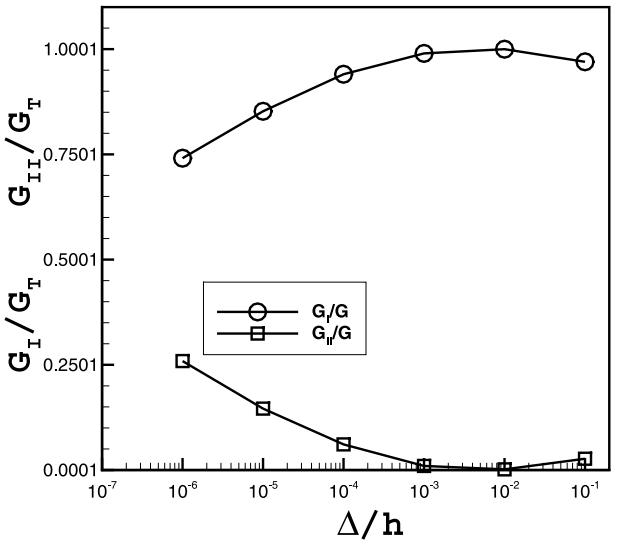

Fig. 11. Results of the p-version finite element analysis of the laminate Fig 7(a) when the first two layers are graphite–epoxy composites and the last layer is graphite–polymer composite.

two layers in a laminate are usually weakly dissimilar. Thus, the mode-separated energy release rates for the interlaminar crack of such a laminate virtually converge.

- However, if two layers are highly dissimilar like case (C), then the oscillating factor becomes large and hence the energy release rates for the Mode I and Mode II do not exist. In other words, the mode-separated energy release rates for the interlaminar cracks of such a highly mismatched bimaterial do not converge.

6. Concluding remarks

By no means is our method able to change the physical property of dissimilar materials so that the oscillating factor can be removed. In other words, neither PAM nor EAM is able to alter the oscillating behavior of the solutions even though it can remove the monotone singularity of type r^{λ} for accurate finite element analysis.

In this paper, we considered only the PAM to deal with the singularities. If the oscillating factor is very large (not realistic), we can take advantage of the EAM to have more accurate finite element analysis. However, EAM transforms a bounded domain Ω_S into unbounded domain $\hat{\Omega}_S$. Moreover, the nonconvergence of mode-separated energy release rates are not due to an inaccuracy of the FE solutions of the displacement vectors, but due to the nature of high mismatch of two dissimilar materials.

Finally, let us note that in the framework of h-FEM, the mapping method introduced in this paper cannot have any advantages over the conventional finite element methods that uses the quarter-point singularity elements around the crack tip (see Appendix A.1 for details).

Acknowledgements

The author thanks Drs. K. O'Brien and I. Raju for inviting him to NASA Langley Research Center for this research. He also thanks Prof. L. Carlsson for personal correspondence related to this research and encouragement. Furthermore, the author is grateful to referees who provide constructive suggestions and comments to improve this paper.

Appendix A

A.1. The method of auxiliary mapping

Babuška and Oh [1,13,14] introduced a new method, called the method of auxiliary mapping (MAM), that can effectively handle the r^{α}-type ($\alpha < 1$) singularities [7,9].

The essence of this method involves locally transforming a neighborhood Ω_S of each singularity point to a new domain $\hat{\Omega}_S$ by use of the mappings such as $z = \zeta^{\beta}$ (the power auxiliary mapping), where $z = x + \mathrm{i}y$, $\zeta = \hat{x} + \mathrm{i}\hat{y}$.

Here β is directly determined by the known nature of the singularity in such a way as to locally transform the exact (singular) solution to a smoother function, which can be easily approximated in the new mapped domain by the conventional use of the p-version of the FEM. An optimal choice for the mapping size β is $1/\alpha$. For example, consider a crack singularity of the form $r^{1/2}f(r,\theta)$ located at the origin, where f is smooth. Then, the auxiliary mapping $\psi(z) = z^{1/4}$ maps the upper half plane into one half of the first quadrant, and a point $(\hat{r},\hat{\theta})$ in the lower half of the first quadrant evaluates as $\hat{r}^2 f(\hat{r}^4, 4\hat{\theta})$, a smooth function.

To further understand the effect of the power auxiliary mapping $\psi(z) = z^{1/4}$, let $\Omega_S = \{(r,\theta) : r < R_1, 0 \leqslant \theta \leqslant \pi/4\}$. Then $\hat{\Omega}_S = \psi(\Omega_S) = \{\hat{r},\hat{\theta}) : \hat{r} \leqslant R_1^{1/4}, 0 \leqslant \hat{\theta} \leqslant \pi/16\}$. If we consider the basis function of p-degree 12 over $\hat{\Omega}_S$, the singular functions created over Ω_S through the power auxiliary mapping restricted to the positive x-axis are generated by $\{1, x^{1/4}, x^{1/2}, x^{3/4}, x, x^{5/4}, \ldots, x^{11/4}, x^3\}$. That is, the auxiliary mapping implicitly creates special singular basis functions which mimic the singularity.

Suppose we use the linear basis functions over $\hat{\Omega}_S$, the singular functions created over Ω_S through the PAM, $\psi(z) = z^{1/2}$, restricted to the positive x-axis are generated by $\{1, x^{1/2}\}$. Thus, it has no more advantage

over the quarter-point singularity elements in h-FEM. Moreover, if the PAM $\psi(z) = z^{1/4}$ were selected, the results would be worse. Thus, the mapping method is not recommended in h-FEM.

A.1.1. Basis vectors for the displacement vector space

The finite element solution of (7) for a specific mesh Δ is to construct approximations of each components of $\{u\}$. Let $\{\Phi_i(x,y) : i = 1,\ldots,n = N(\Delta)\}$ be basis functions of the finite element space $S^p(\Omega,\Delta,\{\Psi_i\})$ which is defined in Section 3. Then the components of a displacement vector (which is in $[S^p(\Omega,\Delta,\{\Psi_i\})]^2$) in term of the basis functions Φ_i are of the form

$$u_x(x,y) = \sum_{i=1}^{n} a_i \Phi_i(x,y),$$

$$u_y(x,y) = \sum_{i=1}^{n} a_{n+i} \Phi_i(x,y),$$

where a_i $(i = 1,\ldots,2n)$ are called the amplitudes of the basis functions Φ_i.

Let

$$\{\Phi\}_i = \begin{Bmatrix} \Phi_i(x,y) \\ 0 \end{Bmatrix}, \quad i = 1,2,\ldots,n; \tag{A.1}$$

$$\{\Phi\}_i = \begin{Bmatrix} 0 \\ \Phi_{i-n}(x,y) \end{Bmatrix}, \quad i = n+1, n+2,\ldots,2n. \tag{A.2}$$

Then $\{u\}$ can be written as

$$\{u\} = \sum_{i=1}^{2n} a_i \{\Phi\}_i.$$

Moreover, we have the following.

Lemma A.1. *The bilinear form (the principal of virtual work) $\mathscr{B}(\{\Phi\}_i,\{\Phi\}_j)$ on an element E becomes*

$$\int_E (\nabla\Phi_j)^{\mathrm{T}} \begin{bmatrix} E_{11} & E_{13} \\ E_{31} & E_{33} \end{bmatrix} \nabla\Phi_i \,\mathrm{d}x\,\mathrm{d}y \quad \text{if } \{v\} = \{\Phi_j, 0\}^{\mathrm{T}},\ \{u\} = \{\Phi_i, 0\}^{\mathrm{T}},$$

$$\int_E (\nabla\Phi_j)^{\mathrm{T}} \begin{bmatrix} E_{33} & E_{32} \\ E_{23} & E_{22} \end{bmatrix} \nabla\Phi_i \,\mathrm{d}x\,\mathrm{d}y \quad \text{if } \{v\} = \{0, \Phi_j\}^{\mathrm{T}},\ \{u\} = \{0, \Phi_i\}^{\mathrm{T}},$$

$$\int_E (\nabla\Phi_j)^{\mathrm{T}} \begin{bmatrix} E_{13} & E_{12} \\ E_{33} & E_{32} \end{bmatrix} \nabla\Phi_i \,\mathrm{d}x\,\mathrm{d}y \quad \text{if } \{v\} = \{\Phi_j, 0\}^{\mathrm{T}},\ \{u\} = \{0, \Phi_i\}^{\mathrm{T}},$$

$$\int_E (\nabla\Phi_j)^{\mathrm{T}} \begin{bmatrix} E_{31} & E_{33} \\ E_{21} & E_{23} \end{bmatrix} \nabla\Phi_i \,\mathrm{d}x\,\mathrm{d}y \quad \text{if } \{v\} = \{0, \Phi_j\}^{\mathrm{T}},\ \{u\} = \{\Phi_i, 0\}^{\mathrm{T}}.$$

A.1.2. Change of variable by the power auxiliary mapping

Let $\varphi^{\beta}_{\mathrm{pow}}(\hat{x},\hat{y})$ is a conformal mapping from the $\hat{x}$–$\hat{y}$ plane to the x–y plane defined by

$$\varphi^{\beta}_{\mathrm{pow}}(\hat{r},\hat{\theta}) = (\hat{r}^{\beta}\cos(\beta\hat{\theta}), \hat{r}^{\beta}\sin(\beta\hat{\theta})), \tag{A.3}$$

where $(\hat{r},\hat{\theta})$ is the polar coordinates of $(\hat{x},\hat{y})$ and the real number $\beta \geqslant 1$ is the mapping size. Let $\nabla_x \equiv (\partial/\partial x, \partial/\partial y)$, $\nabla_{\hat{x}} \equiv (\partial/\partial\hat{x}, \partial/\partial\hat{y})$, and $\{\hat{u}\} = \{u\} \circ \varphi^{\beta}_{\mathrm{pow}}$.

Then the principal of virtual work on Ω_{S} is transformed to the those in the following lemma by the power auxiliary mapping. For the proof, we refer [14].

Lemma A.2 (Change of variables). *Suppose* $\{u\} = \{\Phi_i, 0\}^{\mathrm{T}}$ *and* $\{v\} = \{\Phi_j, 0\}^{\mathrm{T}}$. *Then*

$$\begin{aligned}\mathscr{B}(\{u\},\{v\}) &\equiv \int_{\Omega_{\mathrm{S}}} (\nabla_x \Phi_j)^{\mathrm{T}} \begin{bmatrix} E_{11} & E_{13} \\ E_{31} & E_{33} \end{bmatrix} (\nabla_x \Phi_i)\,\mathrm{d}x\,\mathrm{d}y = \int_{\Omega_{\mathrm{S}}} (\nabla_x \Phi_j)^{\mathrm{T}} \begin{bmatrix} a_{11} & a_{12} \\ a_{21} & a_{22} \end{bmatrix} (\nabla_x \Phi_i)\,\mathrm{d}x\,\mathrm{d}y \\ &= \int_{\hat{\Omega}_{\mathrm{S}}} (\nabla_{\hat{x}} \hat{\Phi}_j)^{\mathrm{T}} \begin{bmatrix} q_{11} & q_{12} \\ q_{21} & q_{22} \end{bmatrix} (\nabla_{\hat{x}} \hat{\Phi}_i)\,\mathrm{d}\hat{x}\,\mathrm{d}\hat{y} \equiv \hat{\mathscr{B}}(\{\hat{u}\},\{\hat{v}\}),\end{aligned} \tag{A.4}$$

where

$$\begin{cases} t = (1-\beta)\hat{\theta}, \\ q_{11} = a_{11}\cos^2 t + a_{22}\sin^2 t - (a_{21}+a_{12})\sin t\cos t, \\ q_{12} = (a_{11}-a_{22})\sin t\cos t - a_{21}\sin^2 t + a_{12}\cos^2 t, \\ q_{21} = (a_{11}-a_{22})\sin t\cos t - a_{12}\sin^2 t + a_{21}\cos^2 t, \\ q_{22} = a_{11}\sin^2 t + a_{22}\cos^2 t + (a_{12}+a_{21})\sin t\cos t. \end{cases}$$

For $\{v\} = \{\Phi_j, 0\}^{\mathrm{T}}$ *and the source vector* $\{f_x, f_y\}^{\mathrm{T}}$, *we have*

$$\mathscr{F}(\{v\}) \equiv \int_{\Omega_{\mathrm{S}}} f_x(x,y)\Phi_j(x,y)\,\mathrm{d}x\,\mathrm{d}y = \int_{\hat{\Omega}_{\mathrm{S}}} \beta^2(\hat{x}^2+\hat{y}^2)^{\beta-1}\hat{f}_x(\hat{x},\hat{y})\hat{\Phi}_j(\hat{x},\hat{y})\,\mathrm{d}\hat{x}\,\mathrm{d}\hat{y} \equiv \hat{\mathscr{F}}(\{\hat{v}\}). \tag{A.5}$$

A.1.3. Elemental mappings of blending type for curved elements

Let $\Omega^{(\mathrm{t})}_{\mathrm{st}}$ be the standard triangular element in the ξ–η plane with vertices $V^{(\mathrm{t})}_1 = (-1,0)$, $V^{(\mathrm{t})}_2 = (1,0)$, $V^{(\mathrm{t})}_3 = (0,\sqrt{3})$.

Then

$$L_1 = (1-\xi-\eta/\sqrt{3})/2,$$

$$L_2 = (1+\xi-\eta/\sqrt{3})/2,$$

$$L_3 = \eta/\sqrt{3}$$

are the nodal basis functions on $\Omega^{(\mathrm{t})}_{\mathrm{st}}$ and represent the area coordinates of $(\xi,\eta) \in \Omega^{(\mathrm{t})}_{\mathrm{st}}$.

Let $\Omega^{(\mathrm{q})}_{\mathrm{st}}$ be the standard quadrilateral element in the ξ–η plane with vertices $V^{(\mathrm{q})}_1 = (-1,-1), V^{(\mathrm{q})}_2 = (1,-1), V^{(\mathrm{q})}_3 = (1,1), V^{(\mathrm{q})}_4 = (-1,1)$. Then

$$N_1 = (1-\xi)(1-\eta)/4,$$
$$N_2 = (1+\xi)(1-\eta)/4,$$
$$N_3 = (1+\xi)(1+\eta)/4,$$
$$N_4 = (1-\xi)(1+\eta)/4$$

are the nodal basis functions on $\Omega_{\mathrm{st}}^{(\mathrm{q})}$.

Let $(X_1, Y_1) = (0,0), (X_2, Y_2), (X_3, Y_3), \ldots, (X_{28}, Y_{28})$ be the coordinates of the nodes $1, \ldots, 28$ of the mesh of Ω_{S} in Fig. 1, respectively. The coordinates of the corresponding points in $\hat{\Omega}_{\mathrm{S}}$ are denoted by $(\hat{X}_k, \hat{Y}_k), k = 1, \ldots, 24$ (that is, $\varphi^2_{\mathrm{pow}}(\hat{X}_k, \hat{Y}_k) = (X_k, Y_k)$). Then, by using the blending function method of Section 6.3.3 of [23], one can construct bijective elemental mappings from the reference elements to the curved elements $\hat{E}_k$.

(A) *Elemental mapping from $\Omega_{\mathrm{st}}^{(\mathrm{t})}$ onto a curved triangular elements with one circular curvy side.*

For example, since $(\hat{r}_3, \hat{\theta}_1)$ and $(\hat{r}_3, \hat{\theta}_2)$ are the polar coordinates of $(\hat{X}_2, \hat{Y}_2)$ and $(\hat{X}_3, \hat{Y}_3)$, the curved side $\hat{S}_1^{(1)} \equiv \overline{2 \to 3}$ of the curved triangle $\hat{E}_1 \equiv \overline{2 \to 3 \to 1}$ is parameterized as follows:

$$\left(\hat{x}_1^{(1)}(\xi), \hat{y}_1^{(1)}(\xi)\right) = \left(\hat{r}_3 \cos\left[\frac{\hat{\theta}_2 - \hat{\theta}_1}{2}(\xi+1) + \hat{\theta}_1\right], \hat{r}_3 \sin\left[\frac{\hat{\theta}_2 - \hat{\theta}_1}{2}(\xi+1) + \hat{\theta}_1\right]\right),$$

where $-1 \leqslant \xi \leqslant 1$. Then the elemental mapping of blending type $\hat{\Phi}_1 : \Omega_{\mathrm{st}}^{(\mathrm{t})} \to \hat{E}_1$ is defined by

$$\begin{aligned}
\hat{x} &= L_1\hat{X}_2 + L_2\hat{X}_3 + L_3\hat{X}_1 + \frac{4L_1L_2}{1-\xi}\left[\hat{x}_1^{(1)}(\xi) - \left(\frac{1-\xi}{2}\hat{X}_2 + \frac{1+\xi}{2}\hat{X}_3\right)\right], \\
\hat{y} &= L_1\hat{Y}_2 + L_2\hat{Y}_3 + L_3\hat{Y}_1 + \frac{4L_1L_2}{1-\xi}\left[\hat{y}_1^{(1)}(\xi) - \left(\frac{1-\xi}{2}\hat{Y}_2 + \frac{1+\xi}{2}\hat{Y}_3\right)\right].
\end{aligned} \tag{A.6}$$

(B) *Elemental mapping from $\Omega_{\mathrm{st}}^{(\mathrm{q})}$ onto a curved quadrilateral elements with two circular curvy sides.*

For instance, suppose $\hat{E}_9 \equiv \overline{3 \to 2 \to 11 \to 12}$ is the curved quadrilateral element with two curved sides in Fig. 1. Then, since the polar coordinates of $(\hat{X}_{11}, \hat{Y}_{11})$ and $(\hat{X}_{12}, \hat{Y}_{12})$, respectively, are $(\hat{r}_2, \hat{\theta}_1)$ and $(\hat{r}_2, \hat{\theta}_2)$, the two curved sides $\hat{S}_1^{(9)} \equiv \overline{3 \to 2}$ and $\hat{S}_3^{(9)} \equiv \overline{11 \to 12}$ are, respectively, parameterized as follows:

$$\left(\hat{x}_1^{(9)}, \hat{y}_1^{(9)}\right)(\xi) = \left(\hat{x}_1^{(1)}, \hat{y}_1^{(1)}\right)(\xi),$$
$$\left(\hat{x}_3^{(9)}, \hat{y}_3^{(9)}\right)(\xi) = \left(\hat{r}_2 \cos\left[\frac{\hat{\theta}_2 - \hat{\theta}_1}{2}(\xi+1) + \hat{\theta}_1\right], \hat{r}_2 \sin\left[\frac{\hat{\theta}_2 - \hat{\theta}_1}{2}(\xi+1) + \hat{\theta}_1\right]\right),$$

where $-1 \leqslant \xi \leqslant 1$. Hence the elemental mapping of blending type $\hat{\Phi}_9 : \Omega_{\mathrm{st}}^{(\mathrm{q})} \to \hat{E}_9$ is defined by

$$\begin{aligned}
\hat{x} &= \hat{x}_1^{(9)}(\xi)\frac{1-\eta}{2} + \hat{x}_3^{(9)}(\xi)\frac{1+\eta}{2}, \\
\hat{y} &= \hat{y}_1^{(9)}(\xi)\frac{1-\eta}{2} + \hat{y}_3^{(9)}(\xi)\frac{1+\eta}{2}.
\end{aligned} \tag{A.7}$$

(C) *Elemental mapping from $\Omega_{\mathrm{st}}^{(\mathrm{q})}$ onto a curved quadrilateral elements with one circular curvy side.*

For example, let $E_{25} \equiv \overline{21 \to 20 \to 29 \to 30} \subset [-h_0, h_0] \times [-h_0, h_0]$ is the curved quadrilateral element with one curved side (see Fig. 1), which is in the regular zone Ω_{R}. Then the curved side $S_1^{(25)} \equiv \overline{21 \to 20}$ is parameterized as follows:

$$\left(x_1^{(25)}, y_1^{(25)}\right)(\xi) = \left(r_1 \cos\left[\frac{\theta_2 - \theta_1}{2}(\xi+1) + \theta_1\right], r_1 \sin\left[\frac{\theta_2 - \theta_1}{2}(\xi+1) + \theta_1\right]\right),$$

where $-1 \leqslant \xi \leqslant 1$ and $r_1 = h_0/2$. Hence, the elemental mapping $\Phi_{25} : \Omega_{\mathrm{st}}^{(\mathrm{q})} \to E_{25}$ is defined by

$$\begin{aligned} x &= x_1^{(25)}(\xi)\frac{1-\eta}{2} + N_3(\xi,\eta)X_{29} + N_4(\xi,\eta)X_{30}, \\ y &= y_1^{(25)}(\xi)\frac{1-\eta}{2} + N_3(\xi,\eta)Y_{29} + N_4(\xi,\eta)Y_{30}. \end{aligned} \tag{A.8}$$

It could be a lot of extra work to construct the singular basis functions constructed through the above mapping technique for the local stiffness matrices and local load vectors. However, the novelty of our method is avoiding this extra work as follows: instead of construing the singular basis functions in $S^p(\Omega, \Delta(\Omega), \{\Psi_k\})$, we use the transformed bilinear form $\hat{\mathscr{B}}(\cdot,\cdot)$ and linear functional $\hat{\mathscr{F}}(\cdot)$ (the right side integrals in Lemma A.2), which is the conventional FEM to compute local stiffness matrices and local load vectors for the corresponding curved elements $\hat{E}$.

References

[1] I. Babuška, H.-S. Oh, The *p*-version of the finite element method for domains with corners and for infinite domains, Numer. Meth. PDEs. 6 (1990) 371.
[2] J.L. Beuth, Separation of crack extension modes in orthotropic delamination models, Int. J. Frac. 77 (1996) 305.
[3] M. Comninou, The interface crack, ASME J. Appl. Mech. 44 (1977) 631.
[4] M. Comninou, The interface crack in a shear field, ASME J. Appl. Mech. 45 (1978) 287.
[5] M. Comninou, D. Schmueser, The interface crack in a combined tension–compression and shear field, J. Appl. Mech. 46 (1979) 345.
[6] E.E. Gdoutos, Fracture Mechanics: An Introduction, Kluwer Academic Publishers, Dordrecht, 1993.
[7] B. Guo, H.-S. Oh, The *h–p* version of the finite element method for problems with interfaces, Int. J. Numer. Meth. Eng. 37 (1994) 1741.
[8] M. Hyer, Stress Analysis of Fiber-Reinforced Composite Materials, McGraw-Hill, New York, 1998.
[9] T.R. Lucas, H.-S. Oh, The method of auxiliary mappings in the finite element solutions of elliptic boundary value problems contain ing boundary or corner singularities, J. Comp. Phys. 108 (1993) 327.
[10] Q. Meng, D.-J. Lee, X. Zhang, Solution of analytical-variational method on bi-material interface crack and its comparison with experiment, KSME Int. J. 11 (1997) 521.
[11] H.-S. Oh, H.J. Kim, S.J. Lee, The numerical methods for oscillating singularities in elliptic boundary value problems, J. Comp. Phys. 170 (2001) 742.
[12] M.G. Manoharan, C.T. Sun, Starin energy release rates of an interfacial crack between two anisotropic solids under uniform axial strain, Comp. Sci. Technol. 39 (1990) 99.
[13] H.-S. Oh, I. Babuška, The *p*-version of the finite element method for the elliptic problems with interfaces, Comp. Meth. Appl. Mech. Eng. 97 (1992) 211.
[14] H.-S. Oh, I. Babuška, The method of auxiliary mapping for the finite element solutions of plane elasticity problems containing singularities, J. Comp. Phys. 121 (1995) 193.
[15] H.-S. Oh, B.S. Jang, Y. Jou, The weighted Ritz–Galerkin method for elliptic boundary value problems on unbounded domains, Numer. Meth. PDEs 19 (2003) 301.
[16] J. Qu, J.L. Bassani, Cracks on bimaterial and bicrystal interfaces, J. Mech. Phys. Solids 37 (1989) 417.
[17] I.S. Raju, Calculation of strain energy release rates with higher order and singular finite elements, Eng. Frac. Mech. 28 (1987) 254.
[18] I.S. Raju, J.H. Crews Jr., M.A. Aminpour, Convergence of strain energy release rate components for edge-delaminated compositse materials, Eng. Frac. Mech. 30 (1988) 383.
[19] J.R. Rice, Elastic fracture mechanics concepts for interfacial cracks, J. Appl. Mech. 98 (1988) 98.
[20] E.F. Rybicki, M.F. Kanninen, A finite element calculation of stress intensity factors by a modified crack closure integral, Eng. Frac. Mech. 9 (1977) 931.
[21] C.T. Sun, M.G. Manoharan, Starin energy release rates of an interfacial crack between two orthotropic solids, J. Comp. Mater. 23 (1989) 460.
[22] Z. Suo, Singularities, interfaces and cracks in dissimilar anisotropic media, Proc. R. Soc. Lond. A 427 (1990) 361.
[23] B. Szabó, I. Babuška, Finite Element Analysis, Wiley, New York, 1990.

[24] T.C.T. Ting, Effects of change of reference coordinates on the stress analyses of anisotropic elastic materials, Int. J. Solid Struct. 18 (1982) 139.
[25] T.C.T. Ting, Explicit solution and invariance of the singularities at an interface crack in anisotropic composites, Int. J. Solid Struct. 22 (1986) 965.
[26] M. Toya, On mode I and mode II energy release rates of an interface crack, Int. J. Frac. 56 (1992) 345.
[27] J.T. Wang, I.S. Raju, Strain energy release rate formula for skin-stiffener debond modeled with plate elements, Eng. Frac. Mech. 54 (1996) 211.